# The in-plane elastic-plastic response of an incompressible, filled hexagonal honeycomb

H Tankasala*, V S Deshpande[+] and N A Fleck[+]

* Now at School of Mechanical, Aerospace & Automotive Engineering, Coventry University, Priory Street, Coventry CV1 5FB, UK

[+] Cambridge University Engineering Dept., Trumpington St., Cambridge, CB2 1PZ, UK

8 May 2021

## Abstract

Exact solutions are derived for the small-strain, in-plane, elasto-plastic response of a hexagonal honeycomb using slender beam theory; incompressibility of the honeycomb is enforced by filling its voids with an incompressible, inviscid fluid. The honeycomb has sides of equal length, but its inclined struts subtend an angle that can deviate from $120^o$ with respect to the vertical side walls. The relative density is sufficiently small that the struts are slender and can be treated as Euler-Bernoulli beams. Exact solutions are obtained for the elastic moduli and macroscopic yield surface of the rigid, ideally plastic lattice under general in-plane loading: the solutions satisfy equilibrium, compatibility and the constitutive response of each elastic, ideally plastic beam. Prior to conducting an elastic analysis, and a rigid, ideally plastic analysis, initial insight is gained by exploring the vector space of inextensional collapse mechanisms of the pin-jointed, *compressible* version of the hexagonal truss. Two inextensional collapse mechanisms of the compressible honeycomb are identified from the null space of the kinematic matrix. The presence of an incompressible, inviscid fluid in the voids of the honeycomb locks-up one mechanism but the other mechanism survives and generates macroscopic shear strain. Consequently, the incompressible hexagonal honeycomb with rigid joints has a high shear compliance and a low shear strength, with values equal to that of the unfilled, compressible honeycomb. In contrast, macroscopic tensile straining of the incompressible honeycomb requires the stretching of bars in addition to bar-bending, and the tensile modulus and strength of the incompressible honeycomb are thereby elevated. Explicit analytical formulae are derived for the macroscopic tensile modulus and strength of the incompressible honeycomb.

Keywords: lattice materials, hexagonal honeycomb, plasticity, yield surface, kinematic matrix, pin-jointed-truss, collapse mechanisms

## 1. Introduction

Much is known about the elasto-plastic response of unfilled 2D lattices at low relative density, see for example, Gibson and Ashby (1997). Less is known about the mechanics of lattices with a compressible core, and there is a negligible literature on the mechanics of lattices filled with an incompressible medium (fluid or solid) of negligible deviatoric strength. Although an extensive literature exists on the mechanics of unfilled honeycombs (see for example the recent review by Wang (2019)), there is little open literature on honeycombs with an incompressible infill. We begin by summarising some of the main results from the literature on the mechanics of the unfilled honeycomb, and of a honeycomb filled with a compressible solid.

### 1.1 Mechanics of unfilled honeycombs

The mechanics of an *unfilled* hexagonal honeycomb has received much attention within the mechanics community since the pioneering monograph by Gibson and Ashby (1997). Gibson and Ashby made use of simple beam theory in order to analyse the effective properties of a periodic honeycomb in terms of its relative density $\bar{\rho} << 1$. They found that plastic collapse modes involving only hinge rotation (without bar extension) are much weaker than modes that also require bar extension. For example, the shear strength of a regular hexagonal honeycomb $\left(\omega = 30^{o}\right)$ involves plastic hinge formation in inextensional bars such that the macroscopic shear strength scales as $\bar{\rho}^{2}$. In contrast, the hydrostatic tensile strength of the regular honeycomb requires bar plastic stretching and consequently the hydrostatic strength scales as $\bar{\rho}$. Subsequently, analytical and finite element studies have explored the sensitivity of in-plane response to various imperfections such as wavy cell walls or randomly moved nodes, see for example, Chen et al. (1999), Wang and McDowell (2004) and Ronan et al. (2016).

### 1.2 Honeycombs with a compressible in-fill

Honeycombs with empty cells are useful in crash mitigation, and it is to be expected that infilling of the cells by a dissipative core may lead to enhanced crash worthiness. To address this, the elevation in strength and in energy absorption of a metallic sandwich plate by polymer foam filling of a square honeycomb or triangular corrugated core has been assessed by Vaziri et al. (2006). They performed a finite element analysis to determine the degree of enhancement in plate

performance under crushing and impulsive loads by the addition of a polymer foam to the cavities of the lattice core of the sandwich plate. The presence of the foam enhances the core stiffness and increases the compressive buckling strength of the core members by supplying lateral support. However, the performance of the polymer foam core is traded against that of the metal, and the foam-filled core gives negligible advantage over the unfilled core on the basis of a fixed total weight of sandwich beam. Recently, experiments on the low-velocity impact of sandwich panels with a corrugated cores have been performed, with the interspaces of the corrugated core filled with an aluminium alloy foam (Yan et al. (2021)). The presence of the foam core reduced the buckling wavelength of the corrugated core members and thereby elevated the compressive strength of the corrugated core, as predicted previously by Vaziri et al. (2006).

Quasi-static, in-plane compressive tests have also been performed on aluminium honeycombs filled with a polyurethane foam, Mozafari et al. (2015). The presence of the foam core increases the in-plane compressive strength but does not alter the crush mode: crush bands form in both the empty and foam-filled hexagonal honeycomb, with negligible lateral straining parallel to the crush bands. Since polyurethane foam crushes in uniaxial compression with almost vanishing transverse strain (that is the 'plastic Poisson ratio' is close to zero), it is to be expected that there is only a small synergistic strengthening of the crush bands in a hexagonal honeycomb by the presence of the foam. Mozafari et al. (2015) commented that the presence of the foam-filling does not change the deformation mode of the hexagonal honeycomb, yet they observed significant synergistic strengthening. Further studies are needed to relate this synergistic strengthening to the geometry of the hexagonal honeycomb and to the multi-axial, compressive strength of the foam at finite strain. As a first step it is instructive to consider the simpler problem of a hexagonal honeycomb filled by an incompressible solid (or liquid) of vanishing deviatoric strength. It is expected that the presence of an incompressible, inviscid liquid will eliminate the crushing mode of a hexagonal honeycomb as uniaxial straining can no longer occur.

### 1.3 Overview of present study

Our study addresses the small strain, in-plane, elasto-plastic response of a filled hexagonal honeycomb, with bars of thickness $t$ and length $\ell$, as shown in Fig. 1(a). The honeycomb is made *incompressible* by the filling of its voids with an incompressible, inviscid fluid. The inclined bars are at an angle of $\pm\omega$ with respect to the transverse direction; consequently, the honeycomb does not enjoy $120^o$ rotational symmetry, and is transversely isotropic in its elastic response. If the

hexagon is regular (that is, the bars are of equal thickness and length, and the angles subtended at the joints are all $120^o$) then the in-plane elastic properties are isotropic. The novelty of the present study lies in the fact that the filling of the voids of the honeycomb by an inviscid, *incompressible* fluid constrains the volume $V$ of each honeycomb cell to be constant.

A fresh examination of the basic mechanics of the *filled* honeycomb is warranted in order to explore the degree to which incompressibility locks up some of the deformation modes of the empty honeycomb under general in-plane loading. Fluid-filled honeycombs exist in practical applications ranging from honey-filled beeswax honeycombs to the local reinforcement of aluminium honeycomb by the potting of elastomeric adhesives in aerospace applications. Additionally, the in-plane response of the filled hexagonal honeycomb sheds light on the multi-axial response of their 3D counterparts, such as adipose tissue that comprises closed adipose cells filled with low-viscosity lipid oils (Comley and Fleck (2010, 2012)).

The in-plane elastic, ideally plastic response is analysed for the periodic hexagonal honeycomb of Fig. 1(a); the honeycomb is made incompressible by the filling of its hexagonal voids by an incompressible second phase of vanishing shear modulus and shear strength, such as an inviscid, incompressible fluid. We shall show that the response is sensitive to the inclination $\omega$ over the full range $-30^o < \omega < 90^o$ and the behaviour changes dramatically for the special case of $\omega = 30^o$. This is seen immediately from the dependence of the volume $V$ of the hexagonal unit cell upon the inclination $\omega$:

$$V = 2\ell^2 \left(1+\sin\omega\right)\cos\omega \qquad (1.1)$$

This relation is plotted in Fig. 1(b). Note that opposing bars come into contact and jam against each other at the limiting values $\omega = -30^o$ and $\omega = 90^o$. The volume $V$ vanishes at $\omega = 90^o$ and attains a maximum at $\omega = 30^o$. The relation (1.1) can be used to determine the dilatation of the unfilled honeycomb due to a change of inclination $\delta\omega$ but with symmetry maintained and the bar length $\ell$ held fixed: the inclined bars remain equally inclined and the vertical bars remain vertical. Then, this perturbation in $\delta\omega$ from $\omega = 30^o$ gives rise to an incompressible, inextensional mode of deformation, whereas a volume change occurs for any other value of $-30^o < \omega < 90^o$. The case $\omega = 30^o$ also gives an isotropic elastic response for both the unfilled and filled honeycomb.

Initial insight into the elastic and plastic deformation modes of the rigid-jointed hexagonal honeycomb is obtained by analysing the kinematics of the *pin-jointed* hexagonal honeycomb, the so-called 'parent, pin-jointed truss' of the 'daughter, *rigid-jointed* frame'. If the parent, pin-jointed truss possesses inextensional collapse mechanisms that generate macroscopic strain, then the daughter, rigid-jointed frame deforms in a macroscopic elastic manner by elastic, inextensional bar bending. Likewise, macroscopic plastic collapse of the rigid-jointed frame is by inextensional plastic hinge formation. Otherwise, macroscopic elastic and plastic deformation response requires elastic and plastic bar stretching, respectively. Bar stretching is a much stiffer and stronger deformation mode than hinge rotation alone. These fundamental notions are discussed in more detail below and by Deshpande et al. (2001) and by Fleck et al. (2010).

The scope of the study is as follows. The kinematics of an incompressible, pin-jointed hexagonal truss is analysed via the kinematic matrix for the unit cell. Then, analytical expressions for the effective elastic constants of the incompressible honeycomb are obtained as a function of relative density $\bar{\rho}$ and bar inclination $\omega$. In subsequent sections of the paper, the rigid, ideally plastic collapse response of the incompressible honeycomb is obtained in terms of a small number of collapse modes. The calculations are exact in the sense that kinematics, equilibrium and the yield response of the bars are respected. Predictions are made for illustrative examples of filled honeycomb with a focus on $\omega = 20^o$, $30^o$ and $40^o$. Analytical expressions are also obtained for pertinent points on the yield surface. Numerical checks on the exact solutions of the present study were performed via finite element simulations of the macroscopic moduli and yield surfaces. Although the finite element simulations provided a useful numerical check that the development of the present study contains no algebraic errors, explicit comparisons are omitted herein for the sake of brevity.

## 2. The relevance of the pin-jointed hexagonal lattice

The relevance of the macroscopic, inextensional collapse modes of a pin-jointed truss to the macroscopic stiffness and strength of a rigid-jointed frame has been firmly established, see Deshpande et al. (2001) for example. The connection is straightforward, as follows. First, recall that the elastic bending stiffness of a slender beam is much less than its axial stiffness. As an example, consider a uniform, slender beam of length $\ell$, height $t << \ell$, thickness $b$ (into the page), with one end free and the other fully built-in. If the beam is made from a solid of Youngs's modulus $E_S$, then an axial load $T$ at the free end generates an end axial displacement

$u = T\ell/(E_S bt)$ whereas a transverse force $T$ at the free end generates a transverse end displacement $v = 4T\ell^3/(E_S bt^3)$. The ratio of transverse to axial displacement is $v/u = 4\ell^2/t^2$, and consequently $v/u$ much exceeds unity for a slender beam $t/\ell << 1$. The beam can therefore be idealised as a rigid, inextensional bar, with a rotational spring at its built-in end of rotational stiffness $T\ell^2/v = E_S bt^3/4\ell$. In the limit of zero rotational stiffness (that is, upon taking the limit $t/\ell \to 0$), the beam behaves as a pin-jointed bar with free rotation about its end joint. The same argument can be extended immediately to the case of a rigid-jointed framework. Consider a pin-jointed truss with the same arrangement of bars as that of a rigid-jointed frame. The collapse modes of the pin-jointed truss coincide with the deformation modes of the rigid-jointed frame that involve beam rotation but negligible beam extension. If the pin-jointed frame has no such collapse modes, then the only available deformation modes of the rigid-jointed version involve bar extension. In particular, as $t/\ell \to 0$, the rigid-jointed frame has the same kinematics as the pin-jointed truss.

The conclusion is immediate: a pin-jointed lattice with collapse mechanisms that generate macroscopic strain gives rise to a rigid-jointed lattice that deforms by bar bending when subjected to a macroscopic strain state. Such a *bending-dominated* lattice has a low macroscopic stiffness; the macroscopic Young's modulus of such a 2D lattice scales as the cube power of its relative density. Alternatively, if the pin-jointed lattice has no strain-generating collapse mechanisms, then the rigid-jointed lattice is *stretching-dominated* and the macroscopic Young's modulus of such a 2D lattice scales linearly with its relative density. An empty hexagonal honeycomb is a common example of a *bending-dominated* lattice whereas a fully triangulated lattice is a common example of a *stretching-dominated* lattice.

A similar argument applies to the plastic collapse of the beam. Assume rigid, ideally plastic behaviour such that the beam is made from a solid of yield strength $\sigma_{YS}$. Then, the axial strength of the beam equals $T_Y = \sigma_{YS} bt$, and its bending strength under a transverse end load $P_Y$ is $P_Y = \sigma_{YS} bt^2/4\ell$ due to the formation of a plastic hinge at its built-in end. The ratio of bending to axial strength is $P_Y/T_Y = t/4\ell$. Thus, a slender beam has a much lower bending strength than its axial strength, and so the collapse response can by idealised by treating the beam as an inextensional bar with a 'rusty hinge' of bending strength $M_Y = \sigma_{YS} bt^2/4$ at its built-in end. It follows immediately that the macroscopic strength of a rigid-jointed frame can be determined by

treating it as a pin-jointed truss but with rusty joints of bending strength $M_Y = \sigma_{YS} bt^2 / 4$. The collapse mechanisms of the truss with rusty joints are identical to those for a frictionless, pin-jointed truss. If no collapse mechanisms exist for the rusty-jointed truss, then the macroscopic strength of the rigid-jointed frame is dictated by the axial strength of its members. Consequently, a *bending-dominated* lattice has a low macroscopic strength that is dictated by plastic hinge formation in its cell walls, whereas the macroscopic strength of a *stretching-dominated* lattice is dictated by the axial strength of the cell walls.

Our strategy is to determine whether inextensional collapse mechanisms exist for the incompressible *pin-jointed* hexagonal truss and, if they do, whether these mechanisms generate macroscopic strain. To do so, we extend the matrix analysis of Pellegrino and Calladine (1986) to the case of a periodic lattice. A similar methodology has been developed by Hutchinson and Fleck (2006) for a Kagome lattice and for a fully triangular lattice[1]. The methods of matrix analysis draw heavily upon the underlying theory of vector spaces, see for example the very readable monograph by Strang (1980).

### 2.1 Matrix analysis of pin-jointed hexagonal lattice

A matrix analysis is now performed on the kinematics of an *unfilled* pin-jointed hexagonal lattice. Assume that each bar $i$ extends by $e_i$ and the joints $j$ displace by $\boldsymbol{u}^j$. Our aim is to explore whether collapse mechanisms exist and whether any of these collapse mechanisms generate macroscopic strain. It suffices to consider bars 1, 2 and 3 of the unit cell as shown in Fig. 2(a). Remove rigid body translation but prescribe a macroscopic material rotation by assuming that both components of the displacement of joint A vanish, and that the vertical displacement of joint D equals that of joint B:

$$u_1^A = u_2^A = 0 \qquad \text{and} \qquad u_2^D - u_2^B = 0 \tag{2.1}$$

Here, and elsewhere, a superscript denotes the joint under consideration and the subscript denotes the co-ordinate direction (1 or 2). The constraint (2.1ii) is consistent with simple shear along the 1-direction.

[1] Hutchinson and Fleck (2006) also considered long wavelength periodic collapse modes by Bloch-wave analysis. These additional modes do not generate macroscopic strain. Macroscopic strain corresponds to the Cauchy-Born limit.

Now introduce a 5-dimensional joint displacement vector in vector space as

$$d_j = \left(u_1^B, u_2^B, u_1^C, u_2^C, u_1^D\right)^{\mathrm{T}} \tag{2.2}$$

where the superscript T denotes transpose. Then, following Pellegrino and Calladine (1986) and Guest and Hutchinson (2003), the bar extensions $e_i$ of the 3 bars are related to the joint displacements $d_j$ via a kinematic matrix $B_{ij}$ such that

$$B_{ij} d_j = e_i \tag{2.3}$$

Note that $B_{ij}$ is of dimensions *m* x *n* where the number of bars is $m = 3$ and the number of unconstrained joints is $n = 5$, as already noted in (2.2). The repeated subscript *j* in (2.3) denotes summation over *j* = 1, 2.. *n* . The rectangular matrix $B_{ij}$ , of rank *r*, is a linear operator between the domain of joint displacements in $\mathbf{R}^5$, and the range of bar extensions in $\mathbf{R}^3$ space. Direct evaluation of $B_{ij}$ gives

$$B_{ij} = \begin{pmatrix} -\cos\omega & -\sin\omega & \cos\omega & \sin\omega & 0 \\ 0 & -\sin\omega & -\cos\omega & \sin\omega & \cos\omega \\ 0 & 1 & 0 & 0 & 0 \end{pmatrix} \tag{2.4}$$

The row space of $B_{ij}$ gives *r* extensional mechanisms while the null space of $B_{ij}$ gives the subset of inextensional mechanisms. We identify the rank *r*, the row space and the null space by attempting to reduce $B_{ij}$ to echelon form with zeros in the lower-left triangle. In doing so, we reduce $B_{ij}$ to

$$\tilde{B}_{ij} = \begin{pmatrix} -\cos\omega & -\sin\omega & \cos\omega & \sin\omega & 0 \\ 0 & -\sin\omega & -\cos\omega & \sin\omega & \cos\omega \\ 0 & 0 & -\cot\omega & 1 & \cot\omega \end{pmatrix} \tag{2.5}$$

The first 3 columns contain pivots, and we conclude that the rank *r* of matrix $\tilde{B}_{ij}$ (and of $B_{ij}$) equals 3. The column space of $B_{ij}$ is spanned by its first 3 columns and the row space of $B_{ij}$ is spanned by its 3 rows. The null space of $B_{ij}$ has dimension $n - r = 5 - 3 = 2$, and a basis for this subspace is found by following the prescription in Pellegrino and Calladine (1986). Consider $\tilde{B}_{ij} d_j = 0$ with $d_4 = 1$ and $d_5 = 0$, and solve for the 3 unknowns $\left(d_1, d_2, d_3\right)$. The resulting solution

$d_j^{(1)}$ ($j$ = 1-5) gives a vector in the null space. Second, consider $\tilde{B}_{ij} d_j = 0$ with $d_4 = 0$ and $d_5 = 1$, and solve for the 3 unknowns $(d_1, d_2, d_3)$. Then, the resulting solution $d_j^{(2)}$ ($j$ = 1-5) gives a second vector in the null space. Taken together, these define a basis for the null space. Upon making use of (2.5) we obtain

$$d_j^{(1)} = (2\tan\omega, 0, \tan\omega, 1, 0)^{\mathrm{T}} \qquad \text{and} \qquad d_j^{(2)} = (1, 0, 1, 0, 1)^{\mathrm{T}} \tag{2.6}$$

Note that these base vectors are not orthogonal: $d_j^{(1)} d_j^{(2)} \neq 0$ (sum over $j$ =1 to 5). Now replace $d_j^{(1)}$ by a vector $d_j^{(3)} = (-1, 0, 0, -\cot\omega, 1)^{\mathrm{T}}$ which sits within the same plane of the null space but is now orthogonal to $d_j^{(2)}$. Thereby, we identify one choice of orthogonal base vectors $d_j^{(3)}$ and $d_j^{(2)}$ for the 2-dimensional subspace of inextensional mechanisms of $B_{ij}$. Any inextensional mechanism can be written as

$$d_j = \lambda_2 d_j^{(2)} + \lambda_3 d_j^{(3)} \tag{2.7}$$

in terms of scalar components $(\lambda_2, \lambda_3)$.

It remains to determine whether (2.7) generates macroscopic strain of the unfilled, periodic lattice for any choice $(\lambda_2, \lambda_3)$. To proceed, express the macroscopic strain in terms of joint displacements. Assume that the *unfilled* compressible honeycomb is subjected to the macroscopic strain state $(E_{11}, E_{22}, E_{12})$, and assume without loss of generality that the macroscopic rotation rate of the honeycomb is such that direct straining $(E_{11}, E_{22})$ is accompanied by a simple shear strain of magnitude $2E_{12}$. The relative displacement of joint C with respect to the stationary joint A of Fig. 2(a) is compatible with macroscopic strain such that

$$u_1^C - u_1^A = u_1^C = 2E_{12}\ell(1 + \sin\omega) + E_{11}\ell\cos\omega \tag{2.8}$$

and

$$u_2^C - u_2^A = u_2^C = E_{22}\ell(1 + \sin\omega) \tag{2.9}$$

Similarly, the horizontal displacement of joint D with respect to joint B of Fig. 2(a) is compatible with macroscopic strain such that

$$u_1^D - u_1^B = 2E_{11}\ell\cos\omega \tag{2.10}$$

Now eliminate $E_{11}$ from (2.8) by making use of (2.10) to obtain

$$2u_1^C + u_1^B - u_1^D = 4E_{12}\ell\left(1+\sin\omega\right) \tag{2.11}$$

Each component $\left(E_{11}, E_{22}, E_{12}\right)$ can now be expressed in terms of joint displacement via (2.9), (2.10) and (2.11), or in terms of $\left(\lambda_2, \lambda_3\right)$, by making use of (2.7) to give

$$E_{11} = \frac{\lambda_3}{\ell\cos\omega}, \qquad E_{22} = \frac{-\lambda_3\cot\omega}{\ell\left(1+\sin\omega\right)} \qquad \text{and} \qquad E_{12} = \frac{\left(\lambda_2-\lambda_3\right)}{2\ell\left(1+\sin\omega\right)} \tag{2.12}$$

along with the volumetric strain

$$E_{11} + E_{22} = \frac{2\left(\sin\omega-\cos 2\omega\right)}{\ell\sin 2\omega\left(1+\sin\omega\right)}\lambda_3 \tag{2.13}$$

A number of conclusions can be drawn immediately from (2.12) and (2.13):

(i) Each of the inextensional collapse mechanisms $\lambda_2 d_j^{(2)}$ and $\lambda_3 d_j^{(3)}$ generates macroscopic strain.

(ii) The mechanism $\lambda_2 d_j^{(2)}$ generates a macroscopic shear strain $E_{12}$ but vanishing direct strain $\left(E_{11}, E_{22}\right)$, as seen by inspection of (2.12). Consequently, this mechanism is isochoric (volume-conserving) and persists for the case of an incompressible, filled honeycomb.

(iii) In general (that is for $\omega \neq 30^{\circ}$), the mechanism $\lambda_3 d_j^{(3)}$ generates volumetric strain and so this mechanism is locked-up by enforcing incompressibility of the filled honeycomb.

(iv) For the specific choice $\omega = 30^{\circ}$, the pre-multiplier for $\lambda_3$ in (2.13) vanishes and this mechanism becomes isochoric. Consequently, for $\omega = 30^{\circ}$, this mechanism may also be active in an incompressible, filled honeycomb. The activation of this additional mechanism when the hexagon has a maximum volume per unit cell (Fig. 1(b)) is analogous to the fact that a pin-jointed truss can acquire additional infinitesimal mechanisms (and additional states of self-stress) when the length of one member is a maximum. Calladine (1974) considered such 'extremal' geometries in explaining a number of properties of the Buckminster Fuller Tensegrity structure.

The above considerations steer our analysis of the elastic and plastic responses of an incompressible hexagonal honeycomb. In general (that is for $\omega \neq 30^{\circ}$), macroscopic elastic and plastic straining in an arbitrary in-plane direction requires bar stretching. In contrast, macroscopic

shear straining can be accommodated by inextensional bar bending in the elastic case, and by inextensional hinge rotation in the plastic case. For the special choice of $\omega = 30^o$, two inextensional deformation modes now exist: the shear mode, and an additional mode.

## 3. Elastic response

The small-strain elastic responses of a *compressible* unfilled honeycomb and of an *incompressible* filled honeycomb are derived as follows. We emphasise that incompressibility is enforced by filling of the voids within the honeycomb by an incompressible medium that supports vanishing deviatoric stress: either a solid of vanishing shear modulus and strength, or an inviscid liquid. The honeycomb of Fig. 2 is subjected to the macroscopic stress state $\left(\Sigma_{11}, \Sigma_{22}, \Sigma_{12}\right)$, and deforms such that the work-conjugate macroscopic strain is $\left(E_{11}, E_{22}, 2E_{12}\right)$.

First, consider a regular *compressible* honeycomb, such that $\omega = 30^o$: symmetry dictates that it is isotropic with a shear modulus $G_{12}$. Since its Poisson's ratio equals unity, it deforms in an incompressible manner under all macroscopic stress states. Consequently, for this geometry, the compressible and incompressible honeycombs behave in an identical, incompressible manner.

Second, consider the *compressible* honeycomb such that $\omega \neq 30^o$. It is an orthotropic solid with 4 independent elastic constants: two in-plane Young's moduli $E_1$ and $E_2$ in the $x_1$ and $x_2$ directions, respectively, a Poisson ratio $\nu_{12}$ (or, equivalently, $\nu_{21}$ since $E_1\nu_{12} = E_2\nu_{21}$ by reciprocity), and an in-plane shear modulus $G_{12}$. In contrast, for the case of an *incompressible*, filled honeycomb with $\omega \neq 30^o$ we have immediately that $\nu_{12} = \nu_{21} = 1$, and consequently $E_1$ equals $E_2$. Thus, there are two independent elastic moduli $E_1$ and $G_{12}$ in addition to the incompressibility statement $\nu_{12} = \nu_{21} = 1$.

Now focus attention on the *incompressible* filled honeycomb, subjected to general in-plane loading $\left(\Sigma_{11}, \Sigma_{22}, \Sigma_{12}\right)$. As explained above, for $\omega \neq 30^o$, there exist 2 independent moduli: a shear modulus $G_{12}$ and an extensional modulus $\eta \equiv E_1 / 2$, such that

$$\Sigma_{12} = 2G_{12}E_{12} \tag{3.1}$$

and

$$\Sigma_{22} - \Sigma_{11} = \eta\left(E_{22} - E_{11}\right) \tag{3.2}$$

Analytical expressions for $G_{12}$ and $\eta$ can be stated in terms of the Young's modulus $E_S$ of the struts and the relative density $\bar{\rho}$ of the lattice, where

$$\bar{\rho} = \frac{3t}{2\ell}\left[\left(1+\sin\omega\right)\cos\omega\right]^{-1} \tag{3.3}$$

For the compressible, unfilled honeycomb, a macroscopic shear stress $\Sigma_{12}$ generates a macroscopic shear strain $2E_{12}$ with no change in volume; consequently, the shear response of the incompressible, filled honeycomb is identical to that of the compressible, unfilled honeycomb. The requisite formula for the shear modulus $G_{12}$ is given by (4.17) of Gibson and Ashby (1997), and upon making use of (3.3) it reads

$$\frac{G_{12}}{\bar{\rho}^3 E_S} = \frac{8}{81}\left(1+\sin\omega\right)^4 \cos^2\omega \tag{3.4}$$

The cube power-law dependence of $G_{12}$ upon $\bar{\rho}$ indicates that this deformation mode is by bar bending. Additional analysis is needed to determine whether the second deviatoric modulus $\eta$ is dictated by the bending or stretching of struts. We shall show below that the macroscopic modulus $\eta$ is associated with strut stretching and is of magnitude

$$\frac{\eta}{\bar{\rho}E_S} = \frac{\left(\sin\omega - \cos 2\omega\right)^2}{3\left(1+2\sin^2\omega\right)} \tag{3.5}$$

to leading order in $\bar{\rho}$.

The macroscopic modulus $\eta$ of the incompressible hexagonal lattice is obtained, to leading order in $\bar{\rho}$, by considering the pin-jointed version of the incompressible, filled honeycomb as follows. Subject the honeycomb of Fig. 2(b) of unit depth to the macroscopic stress state $\left(\Sigma_{11}, \Sigma_{22}, \Sigma_{12} = 0\right)$; additionally, the incompressible infill is subjected to an internal pressure $p$. The method of sections is used to relate the bar tension $T_3$ in the vertical struts and the bar tensions $T_1 = T_2$ in the inclined struts to the stress state $\left(\Sigma_{11}, \Sigma_{22}, \Sigma_{12} = 0\right)$ and $p$, see Fig. 2(b). Force equilibrium across the horizontal cut X-X dictates that

$$T_3 = 2\ell\left(\cos\omega\right)\left(\Sigma_{22} + p\right) \tag{3.6}$$

Similarly, force equilibrium across a vertical cut Y-Y implies that

$$T_1 \cos\omega_1 = \ell\left(1+\sin\omega\right)\left(\Sigma_{11}+p\right) \tag{3.7}$$

Nodal force equilibrium is satisfied, and consequently

$$T_1 = T_2 \qquad \text{and} \qquad T_3 = 2T_1 \sin\omega \tag{3.8}$$

Upon substituting (3.6) and (3.7) into (3.8) we obtain

$$p = \frac{\cos^2\omega}{\left(\sin\omega-\cos 2\omega\right)}\Sigma_{22} - \frac{\left(1+\sin\omega\right)\sin\omega}{\left(\sin\omega-\cos 2\omega\right)}\Sigma_{11} \tag{3.9}$$

It is instructive to rephrase $\Sigma_{ij}$ in terms of hydrostatic and deviatoric macroscopic stress measures, defined as follows. Introduce a hydrostatic component

$$\Sigma_h = \left(\Sigma_{11}+\Sigma_{22}\right)/2 \tag{3.10}$$

and a deviatoric component

$$\Sigma_d = \left(\Sigma_{22}-\Sigma_{11}\right)/2 \tag{3.11}$$

such that

$$\Sigma_{11} = \Sigma_h - \Sigma_d \qquad \text{and} \qquad \Sigma_{22} = \Sigma_h + \Sigma_d \tag{3.12}$$

Write $\Delta\Sigma_h \equiv \Sigma_h + p$ as the *jump* in hydrostatic tensile stress from its value $-p$ of the infill to its value $\Sigma_h$ of the macroscopic stress. Then, upon making use of (3.9) and (3.10), $\Delta\Sigma_h$ can be related directly to $\left(\Sigma_{22}-\Sigma_{11}\right)$ such that

$$\Delta\Sigma_h \equiv \Sigma_h + p = \frac{\left(1+\sin\omega\right)}{2\left(\sin\omega-\cos 2\omega\right)}\left(\Sigma_{22}-\Sigma_{11}\right) \tag{3.13}$$

We proceed to analyse the elastic response of the struts, along with compatibility between axial straining of the struts and macroscopic strain. The axial strain $\varepsilon_3$ in the vertical struts, and the axial strain $\varepsilon_1$ in the inclined struts are related to the bar tensions by the usual Hooke's law,

$$\varepsilon_3 = T_3/\left(tE_S\right) \qquad \text{and} \qquad \varepsilon_1 = T_1/\left(tE_S\right), \tag{3.14}$$

respectively. The macroscopic strain must be compatible with the axial stain $\varepsilon_3$ in the vertical struts, the axial strain $\varepsilon_1$ in the inclined struts, small rotation $\Delta\omega_1$ of the inclined bar 1, and with a matching rotation $\Delta\omega_2 = -\Delta\omega_1$ of the opposing inclined bar 2.

Compatibility is enforced by writing the relative displacement of joint B with respect to joint A of the honeycomb of Fig. 2(a), such that in the horizontal direction we have

$$-\Delta\omega_1 \sin\omega + \varepsilon_1 \cos\omega = -E_{22}\cos\omega \tag{3.15}$$

while in the vertical direction we have

$$\varepsilon_3 + \Delta\omega_1 \cos\omega + \varepsilon_1 \sin\omega = E_{22}\left(1+\sin\omega\right) \tag{3.16}$$

(Note that we have made direct use of incompressibility $E_{11} = -E_{22}$ on the right-hand side (r.h.s.) of (3.15).) Relations (3.8) and (3.14) taken together imply that $\varepsilon_3 = 2\varepsilon_1 \sin\omega$; thus, (3.15) and (3.16) can be reduced to

$$\varepsilon_3\left(1+2\sin^2\omega\right) = 2E_{22}\left(\sin\omega - \cos 2\omega\right)\sin\omega \tag{3.17}$$

upon elimination of $\Delta\omega_1$. Now express $\varepsilon_3$ in (3.17) in terms of macroscopic stress by making use of (3.6), (3.9) and (3.14i); the resulting expression can be rearranged to the form (3.2) along with our desired result (3.5).

We emphasise that incompressibility of the filled honeycomb reduces the number of elastic moduli to the two deviatoric quantities $G_{12}$ and $\eta$. The modulus $\eta$ is directly related to the Young's modulus $E_1$ in the $x_1$ direction, and Young's modulus $E_2$ in the $x_2$ direction, as follows. First, assume that $\Sigma_{22} = 0$, and write (3.2) in the form $\Sigma_{11} = E_1 E_{11}$ for uniaxial tension in the $x_1$ direction; we note immediately that $E_1 \equiv 2\eta$. Alternatively, assume that $\Sigma_{11} = 0$, and write (3.2) in the form $\Sigma_{22} = E_2 E_{22}$ for uniaxial tension in the $x_2$ direction, and $E_2 \equiv 2\eta = E_1$. The expressions (3.4) and (3.5) for the shear modulus $G_{12}$ and the Young's modulus $E_2 \equiv 2\eta$ are compared graphically in Fig. 3. Both moduli are sensitive to bar inclination $\omega$ over the full range $-30^\circ < \omega < 90^\circ$. The shear modulus $G_{12}$ has a smooth maximum, while the Young's modulus $E_2$ is highly sensitive to the value of $\omega$, for $\omega$ in the vicinity of $\omega = 30^\circ$. In contrast, as $\omega$ is increased to $\omega = 90^\circ$, $E_2$ attains a global maximum while $G_{12}$ drops steeply. The lattice is highly

anisotropic ($G_{12} << E_2$ at small $\bar{\rho}$) unless $\omega$ is close to $30^o$. For the special case of $\omega = 30^o$, the regular honeycomb is isotropic and $E_2 = 4G_{12} = 3\bar{\rho}^3/4$, upon making use of (3.4). Recall that the expression (3.5) for $E_2 \equiv 2\eta$ contains only the linear term in $\bar{\rho}$ and neglects the next higher term of order $\bar{\rho}^3$: a more detailed analysis than that given above is required to obtain this second in term $\bar{\rho}^3$ associated with bar bending. However, there is no need to include this second term as it provides a fractional correction to $E_2$ of order $\bar{\rho}^2$, that is 1% or less for $\bar{\rho} \le 0.1$. The coefficient in front of the leading term in $\bar{\rho}$ in (3.5) vanishes for $\omega = 30^o$ and it is only for $\omega$ close to this value that (3.5) fails.

## 4. Yield locus of rigid, ideally plastic filled lattice

An exact solution is developed for the yield locus of a rigid, ideally plastic hexagonal honeycomb within the context of Euler beam theory for the struts. Since the lattice contains an incompressible infill of zero deviatoric strength the yield surface can be presented in deviatoric stress space $(\Sigma_{12}, \Sigma_{22} - \Sigma_{11})$ for any assumed values of $\omega$ and $\bar{\rho}$. The exact solution satisfies equilibrium between macroscopic stress and bar forces (and moments), compatibility between macroscopic strain and bar deformation (stretching and rotation), and a plastic collapse law whereby the bars behave as Euler beams with isolated plastic hinges that are either extensional or inextensional in behaviour. We shall show that the yield surface comprises a finite set of flat and curved facets, with a vertex existing between some but not all facets. Each facet is associated with particular bars of the unit cell behaving in a rigid manner, and the remaining bars containing extensional or inextensional hinges. The details are made precise below.

For the incompressible honeycomb (excluding the special case $\omega = 30^o$), much of the yield surface is characterised by one bar of the triad shown in Fig. 2(c) behaving in a rigid manner while the other 2 bars are at yield with extensional hinges. A small vertical facet of the yield surface is also present just above the $\Sigma_{12}$ axis. It is associated with macroscopic shear straining such that the vertical bar 3 has inextensional hinges while the inclined bars 1 and 2 are rigid. For the special case of $\omega = 30^o$, the yield surface has 2 flat facets; each is associated with the rotation of bars about inextensional hinges.

### 4.1 Yield response of each bar

Assume that the incompressible, filled hexagonal honeycomb of Fig. 2(a) comprises slender beams made from a rigid, ideally plastic solid of yield strength $\sigma_{YS}$. Write $T$ as the axial tension and $M$ as the moment on any beam cross-section. Then, the structural collapse locus for the Euler-Bernoulli beam cross-section is given by the usual yield function $\Phi(M,T)\le 0$ where (Hodge (1959), and equation (4.84) in Gibson and Ashby (1997))

$$\Phi(M,T)=\frac{|M|}{M_0}+\left(\frac{T}{T_0}\right)^2-1\le 0 \tag{4.1}$$

Here, $T_0=t\sigma_{YS}$ is the axial strength (per unit depth into page), and $M_0=t^2\sigma_{YS}/4$ is the bending strength of the cross-section. The yield surface (4.1) displays a vertex at ($M$ =0, $|T|=T_0$).

We emphasise that the Euler-Bernoulli assumption of rigid behaviour in shear implies that the shear force $S$ on the beam cross-section does not enter the yield function (4.1). Elementary considerations support this for the case of a slender beam, $t/\ell<<1$. Consider, for example, a beam of thickness $t$ and length $\ell$ subjected to $T$=0, with $M=M_0$ at one end and $M=-M_0$ at the other end. Then, the transverse shear force $S$ attains its maximum value $S=2M_0/\ell=T_0t/(2\ell)$. Thus, $S/T_0\le t/(2\ell)<<1$ for a slender beam.

The presence of a small shear force $S$ leads to the formation of an isolated plastic hinge (that bends and extends) at each end of the beam rather than a state of uniform curvature and uniform stretch over the length of the beam; write $\Omega$ as the hinge rotation and $e$ as the hinge extension, and note that they are work-conjugate to $(M,T)$, respectively. Normality of plastic flow on the smooth part of the collapse surface (4.1) dictates that

$$\frac{\dot e}{\dot\Omega}=s\frac{t}{2}\frac{T}{T_0} \tag{4.2}$$

upon introducing the indicator function $s=1$ for $\dot\Omega>0$ and $s=-1$ for $\dot\Omega<0$. The moment $M$ is of the same sign as $\dot\Omega$, and $T$ is of the same sign as $\dot e$. At the vertex, we have ($M=0$, $|T|=T_0$), and the forward cone of normals is restricted to

$$|\dot\Omega|/|\dot e|\le 2/t \tag{4.3}$$

The challenge is to obtain the yield surface $\left(\Sigma_{12}, \Sigma_{22}-\Sigma_{11}\right)$ for the incompressible honeycomb in macroscopic stress space $\Sigma_{ij}$. Place a potentially active plastic hinge at each end of the bars 1, 2 and 3 of Fig. 2(a). When the inequality of (4.1) is satisfied, the hinge is inactive and behaves in a rigid manner. The 3 hinges are adjacent to the central joint B, as sketched in Fig. 2(c). Assume that, at any instant, bar *i* rotates at the rate $\dot{\omega}_i$ (*i* =1, 2 or 3) with respect to the fixed $x_1$-$x_2$ reference frame, while the joint B rotates at the rate $\dot{\omega}_B$. Consequently, the hinge at each end of bar *i* has a rotate rate of

$$\dot{\Omega}_i = \dot{\omega}_i - \dot{\omega}_B \tag{4.4}$$

along with an extension rate $\dot{e}_i = \dot{\ell}_i / 2$. (When the hinge in bar *i* is in a rigid state we have $\dot{\Omega}_i = \dot{e}_i = 0$.) It is clear from elementary considerations that the plastic dissipation of the honeycomb is minimised by taking $\dot{\omega}_B$ to equal the rotation rate $\dot{\omega}_i$ of one of the 3 bars. However, the algebraic presentation below is unified and simplified by initially assuming that the joint B has an independent value $\dot{\omega}_B$ from that of the 3 bars; it is assumed that $\dot{\omega}_B$ equals the value $\dot{\omega}_i$ of one of the 3 bars only later in the analysis.

### 4.2 Kinematics for rigid, ideally plastic collapse of incompressible, filled honeycomb

Write the kinematics of the rigid, ideally plastic honeycomb in terms of rate quantities, as follows. Assume that the filled honeycomb is subjected to the macroscopic strain rate $\left(\dot{E}_{11} = -\dot{E}_{22}, \dot{E}_{22}, \dot{E}_{12}\right)$, and that the macroscopic rotation rate of the honeycomb is consistent with that of simple shear straining, in addition to direct straining. Consequently, the relative velocity of joint C with respect to joint A of Fig. 2(a), written in terms of bar rotation rates $\dot{\omega}_i$ and bar extension rates $\dot{\ell}_i$, is compatible with the macroscopic strain rate such that

$$2\dot{E}_{12}\ell\left(1+\sin\omega\right) - \dot{E}_{22}\ell\cos\omega = -\ell\dot{\omega}_3 + \dot{\ell}_1\cos\omega - \ell\dot{\omega}_1\sin\omega \tag{4.5}$$

and

$$\dot{E}_{22}\ell\left(1+\sin\omega\right) = \dot{\ell}_3 + \ell\dot{\omega}_1\cos\omega + \dot{\ell}_1\sin\omega \tag{4.6}$$

Similarly, the relative velocity of joint D with respect to joint B of Fig. 2(a), written in terms of bar rotation rates $\dot{\omega}_i$ and bar extension rates $\dot{\ell}_i$, is compatible with the macroscopic strain rate such that

$$\ell\left(\dot{\omega}_1+\dot{\omega}_2\right)\cos\omega+\left(\dot{\ell}_1-\dot{\ell}_2\right)\sin\omega=0 \tag{4.7}$$

(assuming that joints D and B share the same vertical velocity, as demanded by simple shear) and

$$-2\dot{E}_{22}\ell\cos\omega=\ell\left(\dot{\omega}_2-\dot{\omega}_1\right)\sin\omega+\left(\dot{\ell}_1+\dot{\ell}_2\right)\cos\omega \tag{4.8}$$

For later use, elimination of $\dot{E}_{22}$ from (4.6) and (4.8) provides:

$$\left(1+3\sin\omega\right)\dot{\ell}_1+\left(1+\sin\omega\right)\dot{\ell}_2+2\dot{\ell}_3=\left(\tan\omega\left(1+\sin\omega\right)-2\cos\omega\right)\ell\dot{\omega}_1-\tan\omega\left(1+\sin\omega\right)\ell\dot{\omega}_2 \tag{4.9}$$

We pay due attention to kinematics, equilibrium and the yield condition (4.1) in order to determine the macroscopic yield surface in stress space $\left(\Sigma_{12},\Sigma_{22}-\Sigma_{11}\right)$. Assume, a priori, that all active collapse modes entail a non-vanishing value for $\dot{\omega}_3$. Unless otherwise stated, we shall take $\dot{\omega}_3=-1$ as the driving term, and note that (4.5)-(4.8) provide 4 relations to help solve for the 7 kinematic unknowns $\left(\dot{\omega}_1,\dot{\omega}_2,\dot{\ell}_1,\dot{\ell}_2,\dot{\ell}_3,\dot{E}_{22},\dot{E}_{12}\right)$. The remaining 3 required equations are obtained by considering equilibrium and normality (4.2). Before proceeding, it is worth noting that if $\left(\dot{\omega}_1,\dot{\omega}_2,\dot{\ell}_1,\dot{\ell}_2,\dot{\ell}_3\right)$ are known, then (4.8) gives $\dot{E}_{22}$, and back-substitution of $\dot{E}_{22}$ into (4.5) gives $\dot{E}_{12}$.

The two compatibility relations (4.7) and (4.9) give similar insight to that in section 2 where the algebraic vector space of the kinematic matrix was addressed. Assume that inextensional collapse mechanisms exist, such that $\dot{\ell}_1=\dot{\ell}_2=\dot{\ell}_3=0$ for the incompressible, periodic honeycomb. First, limit attention to the regular hexagonal honeycomb such that $\omega=30^{\circ}$; then, both (4.7) and (4.9) reduce to $\dot{\omega}_1+\dot{\omega}_2=0$ for any value of $\dot{\omega}_3$. Consequently, two collapse mechanisms exist: (i) $\dot{\omega}_1+\dot{\omega}_2=0$ along with $\dot{\omega}_3=0$, and (ii) $\dot{\omega}_1=\dot{\omega}_2=0$ along with $\dot{\omega}_3\neq 0$. We shall determine the precise nature of these two modes below. Second, consider the general case $\omega\neq 30^{\circ}$. Then, the only solution to (4.7) and (4.9) is $\dot{\omega}_1=\dot{\omega}_2=0$ along with $\dot{\omega}_3\neq 0$. Thus, a single mode of inextensional plastic hinges exists. We shall show below that this mode gives rise to a macroscopic strain rate of simple shear.

### 4.3 Equilibrium

The method of sections is now used to relate the axial forces $T_i$ and shear forces $S_i$ in the 3 bars of Fig. 2(c) to the macroscopic stress state $\left(\Sigma_{11},\Sigma_{22},\Sigma_{12}\right)$ and infill pressure *p*. Make cuts at mid-length of the struts on sections X-X and Y-Y as shown in Fig. 2(b). Symmetry dictates that the bending moment on the cross-section of each bars vanishes at their mid-length. Upon introducing the notation

$$\bar{\Sigma}_{11}\equiv\left(\Sigma_{11}+p\right)\ell\,,\qquad \bar{\Sigma}_{22}\equiv\left(\Sigma_{22}+p\right)\ell\qquad\text{and}\qquad \bar{\Sigma}_{12}\equiv\Sigma_{12}\ell \tag{4.10}$$

and performing routine algebraic manipulation, the method of sections for force equilbrium provides

$$\begin{pmatrix} -\left(1+\sin\omega\right)\sin\omega & \cos^2\omega & \cos\omega \\ \left(1+\sin\omega\right)\cos\omega & \cos\omega\sin\omega & \left(2+\sin\omega\right) \\ \left(1+\sin\omega\right)\sin\omega & -\cos^2\omega & \cos\omega \\ \left(1+\sin\omega\right)\cos\omega & \cos\omega\sin\omega & -\left(2+\sin\omega\right) \\ 0 & 0 & -2\cos\omega \\ 0 & 2\cos\omega & 0 \end{pmatrix}\begin{pmatrix}\bar{\Sigma}_{11}\\ \bar{\Sigma}_{22}\\ \bar{\Sigma}_{12}\end{pmatrix}=\begin{pmatrix}S_1\\ T_1\\ S_2\\ T_2\\ S_3\\ T_3\end{pmatrix} \tag{4.11}$$

Note that, for the filled incompressible lattice, we can only solve for $\left(\Sigma_{12},\Sigma_{22}-\Sigma_{11}\right)$ and for the *jump* in value of hydrostatic stress from that of the infill -*p* to that of the remote hydrostatic stress, $\left(\Sigma_{11}+\Sigma_{22}\right)/2$. This jump in hydrostatic stress is again written as $\Delta\Sigma_h=\left(\left(\Sigma_{11}+\Sigma_{22}\right)/2\right)+p$. Also, note from (4.10) that $\ell\left(\Sigma_{22}-\Sigma_{11}\right)=\bar{\Sigma}_{22}-\bar{\Sigma}_{11}$ and $\ell\Delta\Sigma_h=\left(\bar{\Sigma}_{11}+\bar{\Sigma}_{22}\right)/2$; thus, the solution of $\left(\bar{\Sigma}_{11},\bar{\Sigma}_{22}\right)$ provides us immediately with the values of $\left(\Sigma_{22}-\Sigma_{11}\right)$ and of $\Delta\Sigma_h$. The plastic work rate per unit volume is

$$\dot{W}^p=\left(\Sigma_{22}-\Sigma_{11}\right)\dot{E}_{22}+2\Sigma_{12}\dot{E}_{12} \tag{4.12}$$

and it follows immediately that the plastic strain rate vector $\left(2\dot{E}_{12},\dot{E}_{22}\right)$ is normal to the yield surface in $\left(\Sigma_{12},\Sigma_{22}-\Sigma_{11}\right)$ stress space.

## 5. Collapse mechanisms for which one bar is in the rigid state

The yield surface in macroscopic stress space comprises a series of flat and curved facets. In order to determine each facet we need to assume which bars contain active plastic hinges and which bars are rigid. In general, for $\omega \neq 30^o$, we assume in turn that a single bar 1, 2 or 3 is rigid and the remaining bars are actively yielding with plastic hinges at their ends; we then consider the case where 2 bars are rigid, and only the remaining bar is actively plastic. Our choice of $s_i = \pm 1$ must be consistent with the fact that the plastic work rate is non-negative for each hinge *i*, along with the value of $s_i$ that is consistent with equilibrium and kinematics. Also, satisfaction, or not, of the yield criterion (4.1) must be consistent with the loading on each bar.

We proceed to obtain the facets of the yield surface in the first quadrant of stress space $\left(\Sigma_{12}, \Sigma_{22} - \Sigma_{11}\right)$, for the general case $\omega \neq 30^o$. We find that 3 distinct collapse modes exist as illustrated in Fig. 4(a), with the following features:

(i) *mechanism A*: the vertical bar 3 is rigid, and the other 2 bars have extensional plastic hinges.

(ii) *mechanism B*: the inclined bar 2 is rigid, and the other 2 bars have extensional plastic hinges.

(iii) *mechanism C*: both inclined bars 1 and 2 are rigid, and the vertical bar 3 has *inextensional* plastic hinges.

We find that mechanisms A, B and C define the first quadrant of the yield surface for the geometries $0^o < \omega < 30^o$, whereas only mechanisms B and C are active for $30^o < \omega < 90^o$. For completeness, we include in Fig. 4 the active yield mechanisms for the special case $\omega = 30^o$. Mechanism C is again active, along with a closely related mechanism D for which the inclined bar 2 and vertical bar 3 are rigid, while the inclined bar 1 has *inextensional* plastic hinges. Mechanism D is the same as mechanism C but relates to a different plane of symmetry of the hexagonal lattice (in axes rotated clockwise at $60^o$ to that of the $x_1$-$x_2$ reference frame). Mechanism D replaces mechanism C upon rotating the direction of simple shear by $60^o$ clockwise.

Elementary considerations of reflective symmetry allow us to plot immediately the yield surface in quadrants 2 to 4 from that of quadrant 1. Consequently, there is no need to analyse explicitly the case where the inclined bar 1 is rigid while the other 2 bars have extensional plastic hinges. This mechanism is the mirror image of mechanism B above, and is active in quadrants 2 and 4 of macroscopic stress space.

### 5.1 Mechanism A: vertical bar 3 is rigid

Assume that the vertical bar 3 is rigid such that $\dot{\ell}_3 = \dot{\Omega}_3 \equiv \dot{\omega}_3 - \dot{\omega}_B = 0$ and bar 3 rotates at a prescribed rate, say $\dot{\omega}_3 = -1$; the other 2 bars are at yield, with plastic hinges that satisfy (4.1) and (4.2), recall Fig. 4(a). The objective is to solve for the remaining kinematic quantities $\left(\dot{\omega}_1, \dot{\omega}_2, \dot{\ell}_1, \dot{\ell}_2, \dot{E}_{22}, \dot{E}_{12}\right)$, the bar forces $T_i$ and $S_i$ (in bars $i$ =1-3), the stress state $\left(\bar{\Sigma}_{11}, \bar{\Sigma}_{22}, \bar{\Sigma}_{12}\right)$ and thereby the remote stress measure $\left(\Sigma_{22} - \Sigma_{11}\right)$ and jump in hydrostatic stress $\Delta\Sigma_h$. The trajectory of the yield locus in stress space $\left(\Sigma_{12}, \Sigma_{22} - \Sigma_{11}\right)$ is parameterised by assuming values for the tracking variable $T_1 / T_0 < 0$. The detailed derivation of the solution is given in Appendix A.

As an example of the solution, we plot $\left(\Sigma_{12}, \Sigma_{22} - \Sigma_{11}, \Delta\Sigma_h\right)$ as a function of $T_1 / T_0$ in Fig. 5(a) for $\omega = 20^o$. For the choice $T_1 / T_0 = -1$, we have $\Sigma_{12} = 0$ and $\Sigma_{22} - \Sigma_{11}$ attains its maximum value of the yield locus. Then, as $T_1 / T_0$ is increased from -1 to $T_1 / T_0 = -0.79$, $\Sigma_{12}$ increases from zero and $\Sigma_{22} - \Sigma_{11}$ decreases. Mechanism A terminates when the vertical bar 3 yields at $T_1 / T_0 = -0.79$, and for $T_1 / T_0 > -0.79$ it is replaced by mechanism B. The (curved) facet of the yield locus in $\left(\Sigma_{12}, \Sigma_{22} - \Sigma_{11}\right)$ space for mechanism A and $\omega = 20^o$ is shown in Fig. 6(a), upon recalling that $\ell\left(\Sigma_{22} - \Sigma_{11}\right) = \bar{\Sigma}_{22} - \bar{\Sigma}_{11}$ and $\ell\Sigma_{12} = \bar{\Sigma}_{12}$. Each end of this facet comprises a vertex on the yield surface. One vertex is on the $\Sigma_{22} - \Sigma_{11}$ ordinate axis at $T_1 / T_0 = -1$, and the vertex links mechanism A in the first quadrant of stress space to the reflection of mechanism A in the fourth quadrant. The other vertex is located at the point $T_1 / T_0 = -0.79$ where mechanism B meets mechanism A. The yield surface has also been explored in detail for $\omega = 40^o$. It is found that mechanism A is inactive for this choice of $\omega$, and mechanism B replaces mechanism A for stress states close to the $\Sigma_{12} = 0$ axis.

### 5.2 Mechanism B: inclined bar 2 is rigid

Second, consider the case where bar 2 is rigid, such that $\left(T_2, M_2\right)$ lies within the yield surface (4.1), with $\dot{\ell}_2 = \dot{\Omega}_2 = \dot{\omega}_2 - \dot{\omega}_B = 0$. We proceed to solve for $\left(\dot{\omega}_1, \dot{\omega}_2, \dot{\ell}_1, \dot{\ell}_3, \dot{E}_{22}, \dot{E}_{12}\right)$, the bar forces $T_i$ and $S_i$ (in bars $i$=1-3), the stress state $\left(\bar{\Sigma}_{11}, \bar{\Sigma}_{22}, \bar{\Sigma}_{12}\right)$ and thereby the remote stress

measure $\left(\Sigma_{22}-\Sigma_{11}\right)$ and jump in hydrostatic stress $\Delta\Sigma_h$ by again taking $\dot{\omega}_3=-1$ as the driving term, and by again treating $T_1/T_0$ as the tracking parameter. The full details of the solution are recorded in Appendix B.

We proceed to plot $\left(\Sigma_{12},\Sigma_{22}-\Sigma_{11},\Delta\Sigma_h\right)$ as a function of $T_1/T_0$ in Fig. 5(a) for $\omega=20^{\circ}$, and in Fig. 5(c) for $\omega=40^{\circ}$. We observe that mechanism B is operative over the majority of the $T_1/T_0$ range for both values of $\omega$. The (curved) facet of the yield locus in $\left(\Sigma_{12},\Sigma_{22}-\Sigma_{11}\right)$ space follows immediately, upon making use of $\ell\left(\Sigma_{22}-\Sigma_{11}\right)=\bar{\Sigma}_{22}-\bar{\Sigma}_{11}$ and $\ell\Sigma_{12}=\bar{\Sigma}_{12}$, see Fig. 6.

Consider first the facet of the yield surface for which mechanism B is active, for the choice $\omega=20^{\circ}$. As $T_1/T_0$ increases from -0.79 to -0.002, $\Sigma_{12}$ increases monotonically while $\Sigma_{22}-\Sigma_{11}$ drops to almost zero, see Fig. 5(a). Mechanisms A and B occupy most of the yield surface in Fig. 6(a), with only a very small portion of the yield surface occupied by mechanism C (macroscopic shear straining, with details given below), see the magnified portion of the yield surface at $\Sigma_{22}-\Sigma_{11}$ small and positive in Fig. 6(b). Mechanism B switches in a smooth continuous manner (with no vertex) to mechanism C at the point where the yield surface for mechanism B becomes vertical, that is $\dot{E}_{22}\to 0$.

Second, consider the yield surface for $\omega=40^{\circ}$, as plotted in Fig. 6(c). The yield surface is dominated by mechanism B, and is generated by increasing $T_1/T_0$ from 0.024 to 0.78, see Fig. 5(c). Mechanism C replaces mechanism B at a location very close to the axis of $\Sigma_{22}-\Sigma_{11}=0$, see the magnified view of Fig. 5 (d). The active mechanism of the yield surface switches from mechanism B to C at $T_1/T_0=0.024$, see Fig. 6 (d); the transition is smooth and vertex-free, as was the case for $\omega=20^{\circ}$.

### 5.3 Collapse mechanism C for macroscopic shear straining

Macroscopic shear straining excites a particularly simple collapse mechanism: the vertical bar 3 rotates at a rate $\dot{\omega}_3=-1$ deforms in an inextensional manner $\left(\dot{\ell}_3=0\right)$, with rotational plastic hinges $\left(\dot{\Omega}_3\neq 0\right)$. The inclined bars 1 and 2 are rigid, such that $\dot{\ell}_1=\dot{\ell}_2=\dot{\Omega}_1=\dot{\Omega}_2=0$, recall Fig. 4(a). It is shown in Appendix C that the yield surface comprises a vertical straight line in

$(\Sigma_{12}, \Sigma_{22}-\Sigma_{11})$ stress space, emanating from the point $(\Sigma_{22}-\Sigma_{11})=0$ and $\Sigma_{12}$ given by (C3), and repeated here as

$$\Sigma_{12}^{Y} \equiv \Sigma_{12} = \left(\frac{t}{\ell}\right)^2 \frac{\sigma_{YS}}{4\cos\omega} = \frac{1}{9}\cos\omega\left(1+\sin\omega\right)^2 \bar{\rho}^2 \sigma_{YS}$$

(5.1)

in agreement with the expression (4.29a) of Gibson and Ashby (1997) for the shear strength of an unfilled honeycomb.

The flat, vertical facet of the yield surface for mechanism C is shown in Fig. 5 for the 2 examples, $\omega = 20^{o}$ and $\omega = 40^{o}$. The tension $T_1$ is known immediately in terms of $\bar{\Sigma}_{11}$ (or equivalently in terms of $-\ell(\Sigma_{22}-\Sigma_{11})$) from the second line of the equilibrium statement (4.11). This dependence is included in Fig. 5(b) for $\omega = 20^{o}$ and in Fig. 5(d) $\omega = 40^{o}$. For the choice $\omega = 20^{o}$, $(\Sigma_{22}-\Sigma_{11})$ increases from 0 to 0.019 but $\Sigma_{12}$ remains fixed at $\Sigma_{12}^{Y}$ when $T_1/T_0$ is decreased from 0.026 to -0.002. In similar fashion, for $\omega = 40^{o}$, $(\Sigma_{22}-\Sigma_{11})$ increases from 0 to 0.0084 when $T_1/T_0$ is decreased from 0.036 to 0.024. However, the slope of the $(\Sigma_{22}-\Sigma_{11})$ versus $T_1/T_0$ relation switches sign at the transition from mechanism C to B for $\omega = 40^{o}$, but not for $\omega = 20^{o}$, compare Figs. 5(b) and (d).

The shear mechanism C prevails over a finite range of values of $(\Sigma_{22}-\Sigma_{11})$ up to the transition value $(\Sigma_{22}-\Sigma_{11})_{BC}$ such that the yield mechanism switches from C to B on the yield surface. It is shown in Appendix C that the transition value $(\Sigma_{22}-\Sigma_{11})_{BC}$ is adequately given by (C.5), restated here as

$$\left(\frac{\Sigma_{22}-\Sigma_{11}}{\bar{\rho}^2\sigma_{YS}}\right)_{BC} \approx \frac{(1+\sin\omega)\cos^2\omega}{9\sin\omega} \qquad (5.2)$$

The formula (5.2) is compared with the exact solution in Fig. 7: it is highly accurate and reveals that the active domain of mechanism C drops sharply with increasing $\omega$. The accuracy of the scaling $\Sigma_{12}/\left(\bar{\rho}^2\sigma_{YS}\right)$ and $(\Sigma_{22}-\Sigma_{11})/(\bar{\rho}\sigma_{YS})$ to account for the effect of relative density $\bar{\rho}$ upon yield surface shape is explored in Fig. 8(a) for $\omega = 20^{o}$ and in Fig. 8(b) for $\omega = 40^{o}$. The scaling is excellent, except for a mild sensitivity to the value of $\bar{\rho}$ for mechanism B.

In summary, the yield surfaces for $\omega = 20^o$ and $\omega = 40^o$ are compared in Fig. 6, and indicate that only 3 collapse mechanism are active. However, for both values of $\omega$, mechanism C is active only for macroscopic shear straining, and no vertex is present on the $\Sigma_{12}$ axis. For $\omega = 40^o$, mechanism B dominates the yield surface and a pronounced vertex exists on the $(\Sigma_{22} - \Sigma_{11})$ axis. In contrast, the yield surface for $\omega = 20^o$ is dominated by mechanisms A and B, with a vertex between them, and also on the $(\Sigma_{22} - \Sigma_{11})$ axis. We now turn attention to the special case of $\omega = 30^o$.

## 6. Yield surface for the special case $\omega = 30^o$

The regular hexagonal honeycomb of bar inclination $\omega = 30^o$ is a special case whereby the macroscopic yield surface is due to collapse mechanisms that involve only bar rotation about inextensional plastic hinges. Two such inextensional collapse modes exist for $\omega = 30^o$, as noted in section 2 and as sketched in Fig. 4(b). We shall show below that the collapse locus in $(\Sigma_{12}, \Sigma_{22} - \Sigma_{11})$ stress space has two flat facets:

(i) *mechanism C*: a vertical facet associated with macroscopic shear staining. This segment of the yield surface is given by (5.1) as detailed in section 5 above, and for the case $\omega = 30^o$, (5.1) reduces to

$$\Sigma_{12} = \left(\sqrt{3}/8\right)\bar{\rho}^2\sigma_{YS} \tag{6.1}$$

(ii) *mechanism D*: an inclined straight facet associated with a fixed strain rate direction of $\dot{E}_{22}/\dot{E}_{12} = \sqrt{3}$. This facet satisfies

$$\left(\Sigma_{22} - \Sigma_{11}\right) + \frac{2}{\sqrt{3}}\Sigma_{12} = \frac{1}{2}\bar{\rho}^2\sigma_{YS} \tag{6.2}$$

and is associated with the formation of inextensional plastic hinges in the inclined bar 1; the other inclined bar 2 and the vertical bar 3 both behave in a rigid manner. This solution is identical to the preceding case (i) of macroscopic shear straining, but the mechanism gives rise to shear straining in a direction that is rotated clockwise by 60° with respect to the $x_1 - x_2$ reference frame.

We proceed to derive (6.2) for mechanism D. Although it can be derived simply by a rotation of axes by -60°, we choose to outline the few steps required to write this mechanism in our existing reference frame $x_1$–$x_2$. The bar extensions vanish, $\dot{\ell}_1 = \dot{\ell}_2 = \dot{\ell}_3 = 0$, while $\dot{\omega}_2 = \dot{\omega}_3 = \dot{\omega}_B = -1$. The compatibility relations (4.7) and (4.9) both reduce to $\dot{\omega}_1 = -\dot{\omega}_2$, and relation (4.6) then gives $\dot{E}_{22} = \dot{\omega}_1 / \sqrt{3}$ while (4.5) implies $\dot{E}_{12} = \dot{\omega}_1 / 3$. Consequently, the macroscopic strain rate direction is $\dot{E}_{22} / \left(2\dot{E}_{12}\right) = \sqrt{3}/2$. The hinges in the inclined bar 1 are purely rotational, hence $T_1 = 0$ and $S_1 = 2M_0 / \ell = \sigma_{YS} t^2 / (2\ell)$. Consequently, the equilibrium statement as given by row 1 of (4.11) can be re-phrased to

$$\frac{3}{4}\left(\bar{\Sigma}_{22} - \bar{\Sigma}_{11}\right) + \frac{\sqrt{3}}{2}\bar{\Sigma}_{12} = S_1 = \frac{\sigma_{YS} t^2}{2\ell}. \tag{6.3}$$

Now recall that $\left(\bar{\Sigma}_{22} - \bar{\Sigma}_{11}\right) = \ell\left(\Sigma_{22} - \Sigma_{11}\right)$, and express $t / \ell$ in terms of the relative density $\bar{\rho}$ via (3.3); the desired result (6.2) follows immediately. The resulting yield surface is plotted on Fig. 9. A pronounced vertex exists at the intersection of the two facets at $\left(\Sigma_{12}, \Sigma_{22} - \Sigma_{11}\right) = \left(\left(\sqrt{3}/8\right)\bar{\rho}^2\sigma_{YS}, \bar{\rho}^2\sigma_{YS}/4\right)$, with an additional vertex located at $\left(\Sigma_{12}, \Sigma_{22} - \Sigma_{11}\right) = \left(0, \bar{\rho}^2\sigma_{YS}/2\right)$.

## 7. Closed form expressions for collapse strength

So far, we have focussed on the yield surface for the selected bar inclinations $\omega = \left(20^\circ, 30^\circ, 40^\circ\right)$. The yield surface is plotted on Fig. 10(a) for a much wider range of values of $\omega$, for the choice $\bar{\rho} = 0.05$. Recall from Fig. 8 that the normalisation used for the axes of the yield surface is sufficient to make the yield surface shape almost insensitive to the value of $\bar{\rho}$. The deviatoric biaxial strength $\left(\Sigma_{22} - \Sigma_{11}\right)$ at $\Sigma_{12} = 0$ drops steeply but in a continuous manner with increasing $\omega$ to a minimum value at $\omega = 30^\circ$ whereas the shear strength $\Sigma_{12}^Y$ has a much milder sensitivity to $\omega$. Upon noting that the normalisation of the ordinate is by $\bar{\rho}$ whereas that of the abscissa is $\bar{\rho}^2$, it is clear that the yield surfaces in stress space are highly elongated along the $\left(\Sigma_{22} - \Sigma_{11}\right)$ axis, except for $\omega$ close to $\omega = 30^\circ$, see Fig. 10(b). The yield surfaces in Fig. 10

confirm that mechanisms A, B and C are present for $\omega < 30^o$, while mechanisms B and C exist for $\omega > 30^o$.

An analytical expression for the shear strength of the filled lattice has already been given by (5.1). Analytical expressions are now obtained for the deviatoric biaxial strength $(\Sigma_{22} - \Sigma_{11})$ on the axis $\Sigma_{12} = 0$. Note that the yield surface has a vertex along the $(\Sigma_{22} - \Sigma_{11})$ axis, and the dominant collapse mechanism is mechanism A (vertical bar 3 is rigid) for $\omega = 20^o$ and mechanism B (inclined bar 2 is rigid) for $\omega = 40^o$. We consider each case in turn by reconsidering the analysis of section 5 and taking the limit $\Sigma_{12} \to 0$.

### 7.1 Deviatoric biaxial strength $(\Sigma_{22} - \Sigma_{11})$ for mechanism A ($\Sigma_{12} = 0$)

Limit attention to the case where mechanism A is active for deviatoric biaxial loading: $\omega < 30^o$. The analysis of mechanism A in section 5 and in Appendix A simplifies by noting that the yield surface has a vertex on the ordinate when $\Sigma_{12} = 0$, such that $T_1 = T_2 = -T_0$. Consequently, $S_1 = S_2 = 0$ and the plastic hinges of bars 1 and 2 are at a vertex in $M - T$, as demanded by (4.1). The macroscopic stress state follows from the first 2 rows of the equilibrium statement (4.11), such that

$$-(1+\sin\omega)(\sin\omega)\bar{\Sigma}_{11} + (\cos^2\omega)\bar{\Sigma}_{22} = 0 \tag{7.1}$$

and

$$\cos\omega(1+\sin\omega)\bar{\Sigma}_{11} + (\cos\omega\sin\omega)\bar{\Sigma}_{22} = T_1 = -T_0 \tag{7.2}$$

Inversion gives

$$\frac{\bar{\Sigma}_{11}}{t\sigma_{YS}} = \frac{-\cos\omega}{1+\sin\omega} \qquad \text{and} \qquad \frac{\bar{\Sigma}_{22}}{t\sigma_{YS}} = -\tan\omega \tag{7.3}$$

and consequently

$$\frac{\Sigma_{22}^Y}{\bar{\rho}\sigma_{YS}} \equiv \frac{\Sigma_{22} - \Sigma_{11}}{\bar{\rho}\sigma_{YS}} = \frac{2}{3}(\cos 2\omega - \sin\omega) \tag{7.4}$$

upon making use of (3.3). For later use, we introduce here the notation $\Sigma_{22}^{Y}$ for the uniaxial tensile strength.

Recall that (7.4) is inaccurate at $\omega = 30^{o}$ since (6.3) gives the macroscopic strength for this value of bar inclination. At what value of $\omega$ does (7.4) become inaccurate? It is shown in Appendix D that (7.4) is valid for $\omega$ (in radians) over the range

$$0 \le \omega \le \left( \frac{\pi}{6} - \frac{\bar{\rho}}{\sqrt{3}} \right) \tag{7.5}$$

via the relation (3.3). Consider, as a practical case $\bar{\rho}$ =0.05. Then, (7.4) is valid for $\omega$ in the range of zero to 28$^{o}$. The accuracy of (7.4) within the range of (7.5) is confirmed by plotting the uniaxial tensile strength in the vertical, $x_2$ direction as a function of $\omega$ in Fig. 11. The steep and continuous drop in strength with increasing $\omega$ is evident, as already noted above in relation to Fig. 10.

### 7.2 Deviatoric biaxial strength $(\Sigma_{22} - \Sigma_{11})$ for mechanism B ($\Sigma_{12} = 0$)

Now consider the case where mechanism B is active for deviatoric biaxial loading: $\omega > 30^{o}$. Bar 2 is rigid, while bars 1 and 3 are at yield, with $s_1 = -s_3 = 1$. Consider the limit $\Sigma_{12} \to 0$. The equilibrium relations, as stated in rows 5 and 6 of (4.11), give $S_3 = M_3 = 0$ and

$$\bar{\Sigma}_{22} = \frac{T_3}{2\cos\omega} = \frac{T_0}{2\cos\omega} \tag{7.6}$$

as demanded by the yield condition (B2). Then, the vertical bar 3 is in a state of tensile yield and the associated plastic hinge (4.1) is at the vertex in $M - T$ space. It remains to obtain $\bar{\Sigma}_{11}$. An approximation for $\bar{\Sigma}_{11}$ is obtained in Appendix D such that

$$\frac{\bar{\Sigma}_{11}}{T_0} \approx \frac{\cot\omega}{2(1+\sin\omega)} \tag{7.7}$$

We can now evaluate $(\Sigma_{22} - \Sigma_{11}) = (\bar{\Sigma}_{22} - \bar{\Sigma}_{11})/\ell$ from (7.6) and (7.7) to obtain

$$\frac{\Sigma_{22}^{Y}}{\bar{\rho}\sigma_{YS}} \equiv \frac{(\Sigma_{22} - \Sigma_{11})}{\bar{\rho}\sigma_{YS}} \approx \frac{\sin\omega - \cos 2\omega}{3\sin\omega} \tag{7.8}$$

in terms of relative density $\bar{\rho}$, upon making use of (3.3). Relation (7.8) provides an excellent approximation for the uniaxial tensile strength $\Sigma_{22}^{Y}$ in the regime $\omega > 30^{o}$, see Fig. 11. Again, we note a strong sensitivity of strength to bar inclination in this regime.

## 8. Concluding Discussion

It is clear from the present study that the imposition of incompressibility by in-filling of a hexagonal lattice has a major effect upon its elastic and plastic responses, except for the special case of $\omega = 30^{o}$. For $\omega \neq 30^{o}$, the uniaxial elastic and plastic response of the incompressible honeycomb requires bar stretching and consequently the macroscopic modulus and strength scale with relative density $\bar{\rho}$. In contrast, the shear response requires only bar bending and so the shear modulus scales as $\bar{\rho}^{3}$ while the shear strength scales as $\bar{\rho}^{2}$. This weak shear mode is associated with non-affine deformation of the lattice; if affine deformation were enforced then the resulting values of shear modulus and shear strength would scale with relative density $\bar{\rho}$, and thereby grossly overestimate the true response.

The highly anisotropic elastic and plastic responses for $\omega \neq 30^{o}$ can be traced to the effect of incompressibility upon the number of independent collapse mechanisms of the equivalent, pin-jointed lattice. Recall that, for $\omega \neq 30^{o}$, the imposition of incompressibility reduces the number of collapse mechanisms of the pin-jointed lattice from two to one, and this single collapse mode generates a macroscopic shear strain $E_{12}$. A direct correspondence exists between this collapse mechanism of macroscopic shear of the pin-jointed truss, and the *bending-dominated* elastic and plastic deformation modes of the rigid-jointed lattice.

Analytical expressions for the shear modulus, shear strength, uniaxial modulus and uniaxial strength have all been obtained in the present study. Although the exact solution has been derived for the yield locus under general in-plane loading, it has not been possible to derive simple explicit expressions for all facets of the yield surface. A pragmatic approach is to approximate the yield surface by an ellipse and to make use of analytical expressions for the uniaxial and shear strengths in order to define the ellipse, as follows.

Write $\Sigma_{12}^{Y}$ for the shear yield strength as given by (5.1) for any $\omega$. Then write $\Sigma_{22}^{Y} = \bar{\rho}^{2}\sigma_{YS}/2$ for the uniaxial tensile strength for the special case $\omega = 30^{o}$, recall (6.2).

Alternatively, $\Sigma_{22}^{Y}$ is given by (7.4) for $\omega < 30^{o}$ and by (7.8) for $\omega > 30^{o}$. An elliptical fit to the yield surface is of the form

$$\left( \frac{\Sigma_{22} - \Sigma_{11}}{\Sigma_{22}^{Y}} \right)^2 + \left( \frac{\Sigma_{12}}{\Sigma_{12}^{Y}} \right)^2 - 1 \le 0 \qquad (8.1)$$

The quality of this elliptical approximation of the yield surface can be assessed from a comparison with the exact yield surface for the choices $\omega = \left( 20^{o}, 30^{o}, 40^{o} \right)$, see Fig. 12. Despite the limited accuracy of the elliptical approximation, it serves as a useful practical measure of the yield surface over a wide range of values for $\omega$ and $\bar{\rho}$.

The present study is a first step in the development of constitutive models for filled lattices. It provides the basic reference solution for future studies to determine the sensitivity of macroscopic modulus and yield surface shape to geometric imperfection such as randomly located joints. Also, it is anticipated that elastic (and plastic) buckling modes may intervene to modify the size and shape of the collapse locus.

**Acknowledgements**

The authors are grateful for financial support from the European Research Council in the form of an Advanced Grant (MULTILAT, 669764).

**References**

Calladine, C.R. (1978). Buckminster Fuller's 'Tensegrity' structures and Clerk Maxwell's rules for the construction of stiff frames. *Int. J. Solids and Structs.*, **14**, 161-172.

Chen, C., Lu, T., Fleck, N.A. (1999). Effect of imperfections on the yielding of two-dimensional foams. *J. Mech. and Phys. of Solids*, **47**, 2235-2272.

Comley, K. and Fleck, N. A. (2010). A micromechanical model for the Young's modulus of adipose tissue. *Int. J. Solids and Structs.*, **47**, 2982-2990.

Comley, K. and Fleck, N. A. (2012). The compressive response of porcine adipose tissue from low to high strain rate. *Int. J. Impact Engineering*, **46**, 1-10.

Deshpande, V.S., Ashby, M.F. and Fleck, N.A. (2001). Foam topology: bending versus stretching dominated architectures. *Acta Materialia*, **49(6)**,1035-1040.

Fleck, N.A., Deshpande, V.S. and Ashby, M.F. (2010). Micro-architectured materials: past, present and future. *Proc. Roy. Soc. A (London)*, **466**, 2495-2516.

Gibson, L. J. and Ashby, M. F. (1997). Cellular solids, structure and properties. 2nd. Edn. Cambridge University Press.

Guest, S. D. and Hutchinson, J.W. (2003). On the determinacy of repetitive structures. *J. Mech. and Phys. of Solids*, **51**, 383-391.

Hodge, P.G. (1959). Plastic Analysis of Structures. McGraw-Hill, London.

Hutchinson, R.G. and Fleck, N.A. (2006). The structural performance of the periodic truss. *J. Mech. and Phys. of Solids*, **54**(4), 756-782. DOI: 10.1016/j.jmps.2005.10.008

Mozafari, H., Molatefi, H., Crupi, V., Epasto, G. and Guglielmino, E. (2015). In plane compressive response of foam filled aluminium honeycombs. *J. Composite Materials*, **49**(26), 3215-3228.

Pellegrino, S. and Calladine, C.R. (1986). Matrix Analysis of Statically and Kinematically Indeterminate Frameworks. *Int. J. Solids and Structs*., **22**(4), 409-428.

Ronan, W., Deshpande, V. S. and Fleck, N. A. (2016). The tensile ductility of cellular solids: the role of imperfections. *Int. J. Solids and Structs.*, **102-103**, 200-213.

Strang, G. (1980). Linear algebra and its applications, 2nd edn., Academic Press, New York.

Vaziri, A., Xue, Z. and Hutchinson, J.W. (2006). Metal sandwich plates with polymer foam-filled cores, *J. of Mechanics, Materials and Structures*, **1**(1), 970-127.

Wang, A.-J. and McDowell, D. L. (2004). In-Plane Stiffness and Yield Strength of Periodic Metal Honeycombs, *J. Eng. Mats. and Technol*., **126**, 137-156.

Wang, Z. (2019). Recent advances in novel metallic honeycomb structure. *Composites Part B*, **166**, 731-741.

Yan, L.L., Yu, B., Han, B., Zhang, Q.C., Lu, T.J. and Lu, B.H. (2020). Effects of aluminium foam filling on the low-velocity impact response of sandwich panels with corrugated cores. *J. Sandwich Structs. and Mats*., **22**(4), 929-947.

## Appendix A. Mechanism A, such that vertical bar 3 is rigid

Treat the vertical bar 3 as rigid such that $\dot{\ell}_3 = \dot{\Omega}_3 \equiv \dot{\omega}_3 - \dot{\omega}_B = 0$ and bar 3 rotates at a prescribed rate, say $\dot{\omega}_3 = -1$; the other 2 bars are at yield, with plastic hinges that satisfy (4.1) and (4.2), recall Fig. 4(a). Equation (4.4) implies that

$$\dot{\Omega}_1 = \dot{\omega}_1 - \dot{\omega}_B = \dot{\omega}_1 - \dot{\omega}_3 \qquad \text{and} \qquad \dot{\Omega}_2 = \dot{\omega}_2 - \dot{\omega}_B = \dot{\omega}_2 - \dot{\omega}_3 \ . \tag{A1}$$

Now solve for the remaining kinematic quantities $\left(\dot{\omega}_1, \dot{\omega}_2, \dot{\ell}_1, \dot{\ell}_2, \dot{E}_{22}, \dot{E}_{12}\right)$, the bar forces $T_i$ and $S_i$ (in bars $i$ =1-3), the stress state $\left(\bar{\Sigma}_{11}, \bar{\Sigma}_{22}, \bar{\Sigma}_{12}\right)$ and thereby the remote stress measure $\left(\Sigma_{22} - \Sigma_{11}\right)$ and jump in hydrostatic stress $\Delta\Sigma_h$. It is convenient to determine the yield locus in stress space $\left(\Sigma_{12}, \Sigma_{22} - \Sigma_{11}\right)$ in terms of the tracking variable $T_1 / T_0 < 0$. The shear force $S_1 = 2M_1 / \ell$ follows from the yield condition (4.1) for bar 1, to give

$$\frac{S_1}{T_0} = \frac{1}{2}\frac{t}{\ell} s_1 \left(1 - \left(\frac{T_1}{T_0}\right)^2\right) \tag{A2}$$

where $s_1 = \dot{\Omega}_1 / \left|\dot{\Omega}_1\right| = 1$ in order to give a consistent solution with positive plastic work. The first 2 rows of (4.11) express $\left(S_1, T_1\right)$ in terms of $\left(\bar{\Sigma}_{11}, \bar{\Sigma}_{22}, \bar{\Sigma}_{12}\right)$, and these 2 relations can be rearranged to express $\left(\bar{\Sigma}_{22}, \bar{\Sigma}_{12}\right)$ in terms of $\bar{\Sigma}_{11}$ and $\left(S_1, T_1\right)$ as:

$$2\left(\cos^2\omega\right)\bar{\Sigma}_{22} = \left(1+\sin\omega\right)\left(1+2\sin\omega\right)\bar{\Sigma}_{11} + \left(2+\sin\omega\right)S_1 - \left(\cos\omega\right)T_1 \tag{A3}$$

and

$$2\left(\cos\omega\right)\bar{\Sigma}_{12} = -\bar{\Sigma}_{11}\left(1+\sin\omega\right) - \left(\sin\omega\right)S_1 + \left(\cos\omega\right)T_1 \tag{A4}$$

Now determine $\bar{\Sigma}_{11}$ in terms of $T_1 / T_0$ by considering yield of the inclined bar 2. The yield locus of bar 2 reads

$$\frac{S_2}{T_0} = \frac{1}{2}\frac{t}{\ell} s_2 \left(1 - \left(\frac{T_2}{T_0}\right)^2\right) \tag{A5}$$

in analogous fashion to (A2), and a consistent solution is obtained by taking $s_2 = 1$. Now substitute for $\left(S_2, T_2\right)$ in terms of $\bar{\Sigma}_{11}$ by making use of rows 3 and 4 of (4.11), along with (A3) and (A4). A

quadratic expression for $\bar{\Sigma}_{11}$ results, with an analytical solution in terms of $T_1/T_0$. Back-substitution into (A3) and (A4) gives $\bar{\Sigma}_{22}$ and $\bar{\Sigma}_{12}$, respectively. We omit explicit details here for the sake of brevity; the algebra is straightforward but tedious. At this point in the analysis we have obtained $(S_1, S_2, T_2)$ and $\left(\bar{\Sigma}_{11}, \bar{\Sigma}_{22}, \bar{\Sigma}_{12}\right)$ as a function of the tracking variable $T_1/T_0$.

Normality of plastic flow to the yield surface gives the direction of the macroscopic strain rate vector $\left(2\dot{E}_{12}, \dot{E}_{22}\right)$ immediately. The macroscopic strain rate for mechanism A can also be determined as a function of the tracking variable $T_1/T_0$, with $\dot{\omega}_3$ set (arbitrarily) to $\dot{\omega}_3 = -1$. Normality of plastic flow (4.2) for the 2 hinges in bar 1, and for the 2 hinges in bar 2, demands that

$$\frac{\dot{\ell}_1}{\ell} = 2\frac{\dot{e}_1}{\ell} = s_1 \frac{t}{\ell}\frac{T_1}{T_0}\left(\dot{\omega}_1 - \dot{\omega}_3\right) \quad \text{and} \quad \frac{\dot{\ell}_2}{\ell} = 2\frac{\dot{e}_2}{\ell} = s_2 \frac{t}{\ell}\frac{T_2}{T_0}\left(\dot{\omega}_2 - \dot{\omega}_3\right), \tag{A6}$$

respectively. The 2 compatibility relations (4.7) and (4.9) provide 2 additional relations in order to solve for $\left(\dot{\ell}_1, \dot{\ell}_2, \dot{\omega}_1, \dot{\omega}_2\right)$. First, substitute (A6) into (4.7) to obtain

$$\dot{\omega}_2 = \left(1 - s_2 \frac{t}{\ell}\frac{T_2}{T_0}\tan\omega\right)^{-1}\left[\dot{\omega}_3\left(s_1\frac{T_1}{T_0} - s_2\frac{T_2}{T_0}\right)\frac{t}{\ell}\tan\omega - \dot{\omega}_1\left(1 + s_1\frac{t}{\ell}\frac{T_1}{T_0}\tan\omega\right)\right] \tag{A7}$$

Then, substitute (A6) and (A7) into (4.9) in order to obtain $\dot{\omega}_1$ as a function of $T_1/T_0$. Back substitution into (A7) gives $\dot{\omega}_2$, and into (A6) gives $\left(\dot{\ell}_1, \dot{\ell}_2\right)$. The macroscopic strain rate $\left(\dot{E}_{12}, \dot{E}_{22}\right)$ follows immediately from (4.5) and (4.6).

## Appendix B. Mechanism B such that the inclined bar 2 is rigid

Treat bar 2 as rigid, such that $(T_2, M_2)$ lies within the yield surface (4.1) and $\dot{\ell}_2 = \dot{\Omega}_2 = \dot{\omega}_2 - \dot{\omega}_B = 0$. Equation (4.4) implies that

$$\dot{\Omega}_1 = \dot{\omega}_1 - \dot{\omega}_B = \dot{\omega}_1 - \dot{\omega}_2 \quad \text{and} \quad \dot{\Omega}_3 = \dot{\omega}_3 - \dot{\omega}_B = \dot{\omega}_3 - \dot{\omega}_2 \tag{B1}$$

Now solve for $\left(\dot{\omega}_1, \dot{\omega}_2, \dot{\ell}_1, \dot{\ell}_3, \dot{E}_{22}, \dot{E}_{12}\right)$, the bar forces $T_i$ and $S_i$ (in bars *i*=1-3), the stress state $\left(\bar{\Sigma}_{11}, \bar{\Sigma}_{22}, \bar{\Sigma}_{12}\right)$ and thereby the remote stress measure $\left(\Sigma_{22} - \Sigma_{11}\right)$ and jump in hydrostatic stress $\Delta\Sigma_h$ by again taking $\dot{\omega}_3 = -1$ as the driving term; again, employ $T_1 / T_0$ as the tracking parameter.

The development parallels that given above in (A2)-(A4) as bar 1 is again actively yielding. For any assumed value of $T_1 / T_0$, the shear force $S_1 / T_0$ is determined via (A2), with $s_1 = 1$. Now determine $\bar{\Sigma}_{11}$ in terms of $T_1 / T_0$ by considering yield of the inclined bar 3. Yield of bar 3 implies from (4.1) that

$$\frac{S_3}{T_0} = \frac{1}{2}\frac{t}{\ell} s_3 \left(1 - \left(\frac{T_3}{T_0}\right)^2\right) \tag{B2}$$

and a consistent solution is obtained by taking $s_3 = -1$. Row 5 of (4.11) states that $S_3 = -2\bar{\Sigma}_{12}\cos\omega$ while row 6 states that $T_3 = 2\bar{\Sigma}_{22}\cos\omega$. Upon expressing $\bar{\Sigma}_{22}$ in terms of $\bar{\Sigma}_{11}$ via (A3), and $\bar{\Sigma}_{12}$ in terms of $\bar{\Sigma}_{11}$ via (A4), satisfaction of yield (B2) becomes

$$\left(1 - \frac{2s_3\ell}{tT_0}\left[\left(1+\sin\omega\right)\bar{\Sigma}_{11} + \left(\sin\omega\right)S_1 - \left(\cos\omega\right)T_1\right]\right)\cos^2\omega =$$

$$\left[\left(1 + 3\sin\omega + 2\sin^2\omega\right)\frac{\bar{\Sigma}_{11}}{T_0} + \left(2+\sin\omega\right)\frac{S_1}{T_0} - \cos\omega\frac{T_1}{T_0}\right]^2 \tag{B3}$$

This quadratic expression for $\bar{\Sigma}_{11}$ is solved analytically as a function of $T_1 / T_0$. Back-substitution into (A3) and (A4) gives $\bar{\Sigma}_{22}$ and $\bar{\Sigma}_{12}$, respectively. In summary, we have obtained $\left(S_1, S_3, T_3\right)$ and $\left(\bar{\Sigma}_{11}, \bar{\Sigma}_{22}, \bar{\Sigma}_{12}\right)$ as a function of the tracking variable $T_1 / T_0$.

Now consider the kinematics for this deformation mechanism. Normality of plastic flow (4.2) for the 2 hinges in bar 1, and for the 2 hinges in bar 3, demands that

$$\frac{\dot{\ell}_1}{\ell} = 2\frac{\dot{e}_1}{\ell} = s_1\frac{t}{\ell}\frac{T_1}{T_0}\left(\dot{\omega}_1 - \dot{\omega}_2\right) \quad \text{and} \quad \frac{\dot{\ell}_3}{\ell} = 2\frac{\dot{e}_3}{\ell} = s_3\frac{t}{\ell}\frac{T_3}{T_0}\left(\dot{\omega}_3 - \dot{\omega}_2\right), \tag{B4}$$

respectively. The 2 compatibility relations (4.7) and (4.9) provide 2 additional relations in order to allow us to solve for $\left(\dot{\ell}_1, \dot{\ell}_3, \dot{\omega}_1, \dot{\omega}_2\right)$. First, substitute (B4) into (4.7) to obtain

$$\dot{\omega}_2 = \left( s_1 \frac{t}{\ell} \frac{T_1}{T_0} \tan\omega - 1 \right)^{-1} \left( s_1 \frac{t}{\ell} \frac{T_1}{T_0} \tan\omega + 1 \right) \dot{\omega}_1 \qquad \text{(B5)}$$

Then, substitute (B5) and (B4) into (4.9) in order to obtain $\dot{\omega}_1$ as a function of $T_1 / T_0$. Back substitution into (B5) gives $\dot{\omega}_2$, and into (B4) gives $\left( \dot{\ell}_1, \dot{\ell}_2 \right)$. The macroscopic strain rate $\left( \dot{E}_{12}, \dot{E}_{22} \right)$ follows immediately from (4.5) and (4.6).

## Appendix C: Collapse mechanism C for macroscopic shear straining

Assume that $\dot{\omega}_3 = -1$. The inclined bars 1 and 2 are rigid, such that $\dot{\ell}_1 = \dot{\ell}_2 = \dot{\Omega}_1 = \dot{\Omega}_2 = 0.$ Equation (4.4) then implies that

$$\dot{\omega}_1 = \dot{\omega}_2 = \dot{\omega}_B \qquad \text{and} \qquad \dot{\Omega}_3 = \dot{\omega}_3 - \dot{\omega}_B = \dot{\omega}_3 - \dot{\omega}_2 \neq 0 \qquad \text{(C1)}$$

The compatibility relation (4.7) requires that $\dot{\omega}_1 = \dot{\omega}_2 = 0$, while (4.9) implies that $\dot{\ell}_3 = 0$. The normality statement (4.2) for plastic collapse of the 2 hinges of the vertical bar 3 is of the form (B4ii) and implies that $T_3 / T_0 = 0$. Row 6 of the equilibrium relations (4.11) gives $\bar{\Sigma}_{22} = 0$ while row 5 gives

$$S_3 = -2\bar{\Sigma}_{12} \cos\omega \qquad \text{(C2)}$$

Since $T_3 / T_0 = 0$, the yield condition (A1) for the hinges of bar 3 reduces to $S_3 / T_0 = s_3 t / (2\ell)$; note that $s_3 = -1$ since $S_3$ is negative from (C2). The macroscopic shear stress follows from (C2) as $\bar{\Sigma}_{12} = -T_0 s_3 t / (4\ell \cos\omega)$ or equivalently,

$$\Sigma_{12}^Y \equiv \Sigma_{12} = \left( \frac{t}{\ell} \right)^2 \frac{\sigma_{YS}}{4\cos\omega} = \frac{1}{9} \cos\omega \left( 1 + \sin\omega \right)^2 \bar{\rho}^2 \sigma_{YS} \qquad \text{(C3)}$$

upon making use of the expression (3.3) for relative density. (For later use, we introduce the notation $\Sigma_{12}^Y$ for the macroscopic shear strength.) Thus, the yield surface is a vertical straight line in $\left( \Sigma_{12}, \Sigma_{22} - \Sigma_{11} \right)$ stress space, emanating from the point $\left( \Sigma_{22} - \Sigma_{11} \right) = 0$ and $\Sigma_{12}$ given by (C3). The stress component $\bar{\Sigma}_{11}$ is a free variable, with $\ell \left( \Sigma_{22} - \Sigma_{11} \right) = -\bar{\Sigma}_{11}$ since $\bar{\Sigma}_{22} \equiv 0$ as noted above. Now consider the macroscopic strain rate. Both (4.6) and (4.8) state that $\dot{E}_{22} = 0$ while

(4.5) reduces to $2\dot{E}_{12} = -\dot{\omega}_3 / (1+\sin\omega)$. Thus, the collapse mode is simple shear, as demanded by normality.

The shear mechanism C exists over a finite range of values of $(\Sigma_{22} - \Sigma_{11})$ up to the transition value $(\Sigma_{22} - \Sigma_{11})_{BC}$ such that the yield mechanism switches from C to B on the yield surface. The transition value $(\Sigma_{22} - \Sigma_{11})_{BC}$ is now determined. Consider the yield mechanism C, with $\Sigma_{12}$ stated by (C3) and $\bar{\Sigma}_{22} = 0$. The transition from mechanism B to C occurs when bar 1 begins to yield such that (A2) is satisfied, where $(S_1, T_1)$ are given by rows 1 and 2 of (4.11). Now make use of (C3) for $\Sigma_{12}$ in obtain to an expression for $\Sigma_{11}$ in terms of $(t/\ell)^2$ to leading order. Upon disregarding the higher order terms we obtain

$$\frac{-\Sigma_{11}}{\sigma_{YS}} \approx \frac{1}{4(1+\sin\omega)\sin\omega}\left(\frac{t}{\ell}\right)^2 \qquad \text{(C4)}$$

Thus, the transition value $(\Sigma_{22} - \Sigma_{11})_{BC}$ reads

$$\left(\frac{\Sigma_{22} - \Sigma_{11}}{\bar{\rho}^2 \sigma_{YS}}\right)_{BC} \approx \frac{(1+\sin\omega)\cos^2\omega}{9\sin\omega} \qquad \text{(C5)}$$

upon making use of the relation (2.3) for the relative density $\bar{\rho}$ and by recalling $\bar{\Sigma}_{22} = 0$ for mechanism C.

## Appendix D: Deviatoric strength for mechanisms A and B

**Deviatoric biaxial strength $(\Sigma_{22} - \Sigma_{11})$ for mechanism A ($\Sigma_{12} = 0$)**

We shall now show that the formula (7.4) breaks down at a value of $\omega$ which is slightly less than $30^o$; the breakdown occurs when the loading point on the yield surface for bars 1 and 2 begins to move away from the vertex $T_1 = T_2 = -T_0$. To show this, first note that the uniaxial stress state ($\Sigma_{22} > 0, \Sigma_{11} = 0$) is located at the vertex along the $(\Sigma_{22} - \Sigma_{11})$ axis of macroscopic stress space. The macroscopic straining direction is $\dot{E}_{22} > 0$ and $\dot{E}_{12} = 0$. Symmetry dictates that the vertical bar 3 remains rigid and does not rotate, such that $\dot{\omega}_3 = \dot{\omega}_B = 0$. The two inclined bars deform in the same manner such that $\dot{\ell}_1 = \dot{\ell}_2$ and $\dot{\omega}_1 = -\dot{\omega}_2$. The compatibility relation (4.7) is satisfied identically, while (4.9) demands that

$$\dot{\ell}_1 = \frac{(\sin\omega - \cos 2\omega)}{(1+2\sin\omega)\cos\omega}\,\ell\dot{\omega}_1 \tag{D1}$$

We limit attention to $\omega < 30^{\circ}$, and note from (D1) that $\dot{\ell}_1 < 0$ upon taking $\dot{\omega}_1 > 0$. The direction of plastic straining of the plastic hinges in bars 1 and 2, as specified by (D1), places the loading point at the vertex of (4.1), such that $T_1 = T_2 = -T_0$, and $S_1 = S_2 = M_1 = M_2 = 0$. This is consistent with the fact that the macroscopic stress state places the loading point of the beams 1 and 2 at a vertex of the yield surface. The limiting value of $\left|\dot{\ell}_1\right| / \ell\dot{\omega}_1$ such that the loading point only just remains at the vertex of (4.1) is given by

$$\left(\left|\dot{\ell}_1\right| / \ell\left|\dot{\omega}_1\right|\right) \geq (t/\ell) \tag{D2}$$

and, upon making use of (D1), this limits the value of $\omega$ (in radians) to

$$\omega \leq \frac{\pi}{6} - \frac{2}{3}\frac{t}{\ell} \tag{D3}$$

for small $t/\ell$. Thus, (7.4) is valid for $\omega$ (in radians) over the range of (7.5).

**Deviatoric biaxial strength $(\Sigma_{22} - \Sigma_{11})$ for mechanism B ($\Sigma_{12} = 0$)**

An approximation for $\bar{\Sigma}_{11}$ is obtained as follows. First, note that $\bar{\Sigma}_{11}$ is related to $(S_1, T_1)$ via the equilibrium statement (A4) for bar 1:

$$(1+\sin\omega)\,\bar{\Sigma}_{11} = T_1\cos\omega - S_1\sin\omega \tag{D4}$$

when $\Sigma_{12} = 0$. Now obtain $(S_1, T_1)$. Substitute (7.6) and (D4) into the equilibrium relation (A3) for bar 1 to obtain

$$T_1\sin\omega + S_1\cos\omega = T_0/2 \tag{D5}$$

and make use of the yield equation (A2) for bar 1 to obtain

$$s_1\left(\frac{t}{\ell}\right)\left(\frac{T_1}{T_0}\right)^2\cos\omega - 2\frac{T_1}{T_0}\sin\omega + \left(1 - s_1\frac{t}{\ell}\cos\omega\right) = 0 \tag{D6}$$

This quadratic equation for $T_1$ has the solution

$$\frac{\beta}{\sin\omega}\frac{T_1}{T_0} = 1-\left[1-\frac{\beta(1-\beta)}{\sin^2\omega}\right]^{1/2} \approx \frac{\beta}{2\sin^2\omega} - \frac{\beta^2}{2\sin^2\omega}\left(\frac{4\sin^2\omega-1}{4\sin^2\omega}\right)+\ldots \quad \text{for small } \beta \tag{D7}$$

where

$$\beta = (t/\ell)\, s_1 \cos\omega \tag{D8}$$

For the practical case $(t/\ell) << 1$, the solution (D7) for $T_1$ has the asymptotic form

$$\left(\frac{T_1}{T_0}\right) \approx \frac{1}{2\sin\omega} - \frac{s_1 t}{2\ell}\cot\omega\left(\frac{4\sin^2\omega-1}{4\sin^2\omega}\right) \tag{D9}$$

Now substitute (D9) into (D5) to obtain

$$\left(\frac{S_1}{T_0}\right) \approx \frac{s_1 t}{8\ell}\frac{\left(4\sin^2\omega-1\right)}{\sin^2\omega} \tag{D10}$$

and make use of (D4) to obtain (7.7).

## Figure Captions

Fig. 1 (a) The filled, incompressible hexagonal honeycomb; (b) volume $V$ of unit cell as a function of bar inclination $\omega$ over its full range $0^o < \omega < 90^o$.

Fig. 2. The hexagonal honeycomb. (a) Geometry and in-plane loading; (b) method of sections along planes X-X and Y-Y, and resolved bar forces due to macroscopic direct stress $(\Sigma_{11}, \Sigma_{22})$; (c) forces and moments on a representative joint B, with plastic hinges formed in each of the 3 bars 1, 2 and 3 that meet at this joint.

Fig. 3. Elastic moduli of the filled honeycomb.

Fig. 4. The collapse modes that define the yield surface for (a) $\omega \neq 30^o$ and (b) $\omega = 30^o$.

Fig. 5. Generation of the yield surface by varying $T_1 / T_0$, for (a, b) $\omega = 20^o$ and (c, d) $\omega = 40^o$. Zoomed-in portions of (a) and (c) are shown in (b) and (d), respectively, to reveal the transition between mechanisms B and C. The labels A, B and C indicate the regime of dominance of mechanisms A, B and C, respectively.

Fig. 6. The yield surface and the active mechanisms for $\bar{\rho} = 0.05$. (a) $\omega = 20^o$ and (b) $\omega = 20^o$, enlarged view near shear axis; (c) $\omega = 40^o$ and (d) $\omega = 40^o$, enlarged view near shear axis.

Fig. 7. Dependence of transition value of $(\Sigma_{22} - \Sigma_{11})_{BC}$ for mechanisms B and C upon bar inclination $\omega$, for $\bar{\rho} = 0.05$.

Fig. 8. Sensitivity of yield surface shape to relative density $\bar{\rho}$ for (a) $\omega = 20^o$ and (b) $\omega = 40^o$.

Fig. 9. Collapse surface for the singular case of a regular honeycomb, with $\omega = 30^o$.

Fig. 10. (a) yield surface for a wide range of values of bar inclination $\omega$, for $\bar{\rho} = 0.05$. (b) yield surface size for $\omega$ in the vicinity of $\omega = 30^o$, again for $\bar{\rho} = 0.05$.

Fig. 11. Dependence of uniaxial tensile strength upon bar inclination $\omega$. The relative density is $\bar{\rho} = 0.05$ for the exact solution.

Fig. 12. Approximate fit to the yield surface by an ellipse for (a) $\omega = 20^o$, (b) $\omega = 40^o$ and (c) $\omega = 30^o$. The relative density is $\bar{\rho} = 0.05$ in (a) and (b).

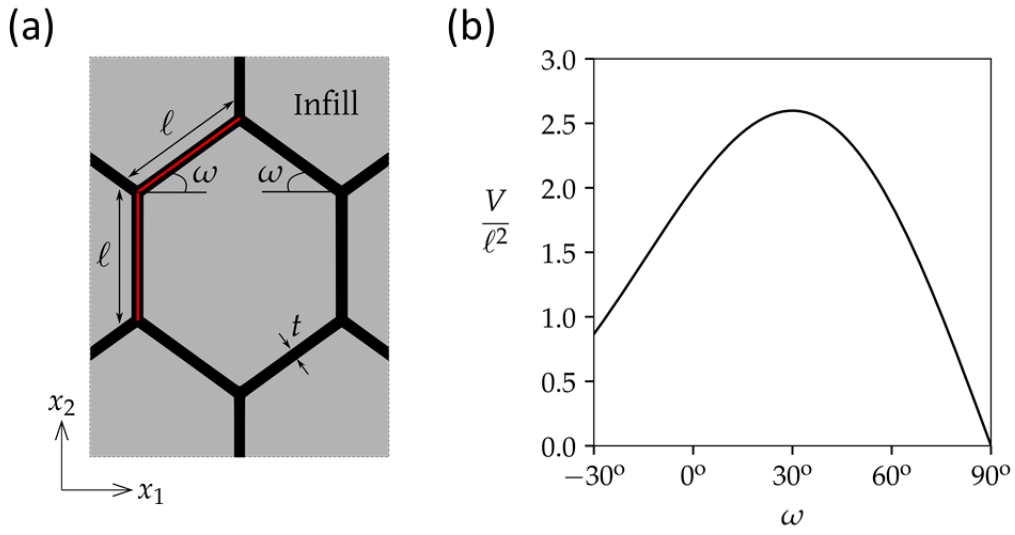


Fig. 1 (a) The filled, incompressible hexagonal honeycomb; (b) volume $V$ of unit cell as a function of bar inclination $\omega$ over its full range $0^o < \omega < 90^o$.

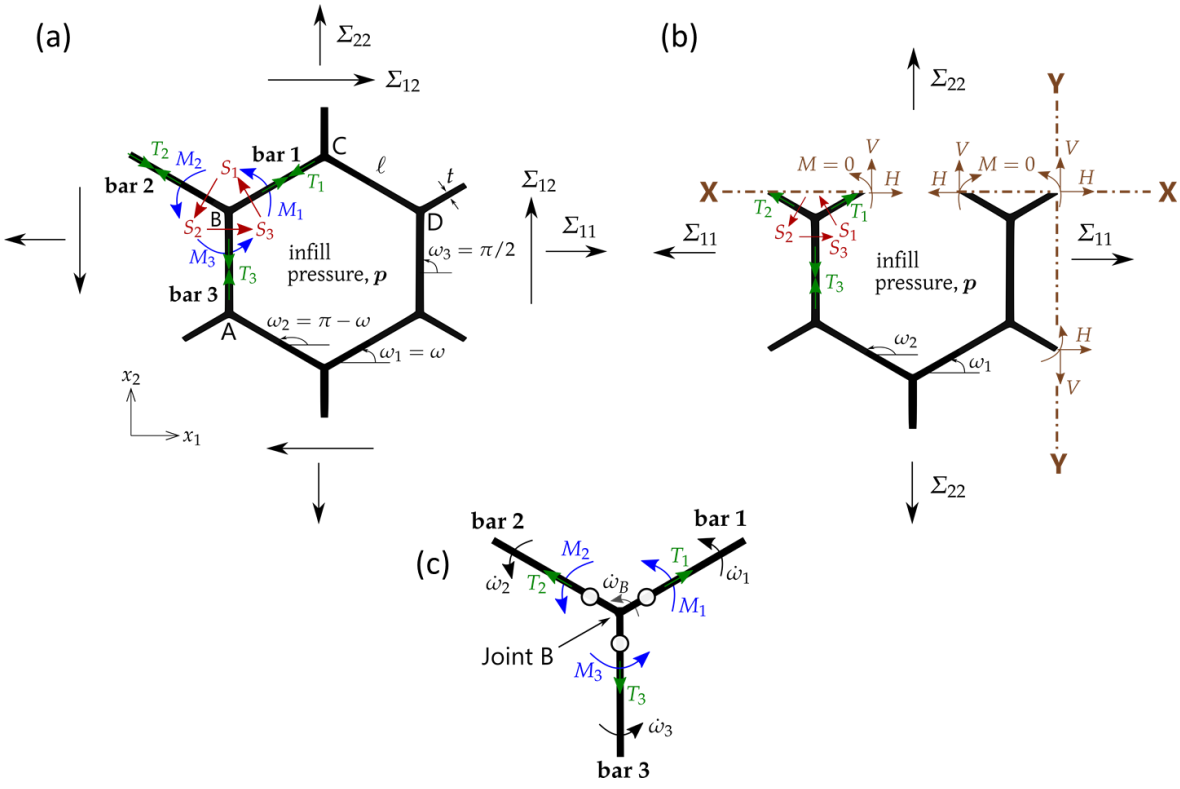


Fig. 2. The hexagonal honeycomb. (a) Geometry and in-plane loading; (b) method of sections along planes X-X and Y-Y, and resolved bar forces due to macroscopic direct stress $(\Sigma_{11}, \Sigma_{22})$; (c) forces and moments on a representative joint B, with plastic hinges formed in each of the 3 bars 1, 2 and 3 that meet at this joint.

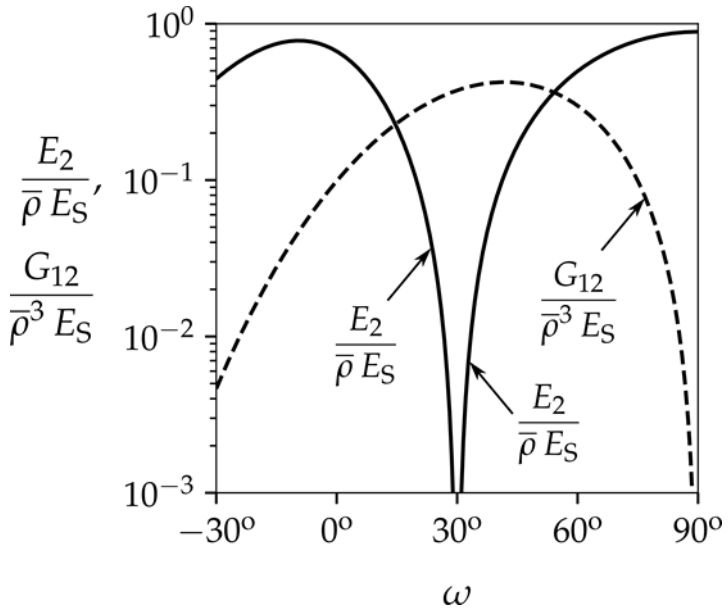


Fig. 3. Elastic moduli of the filled honeycomb.

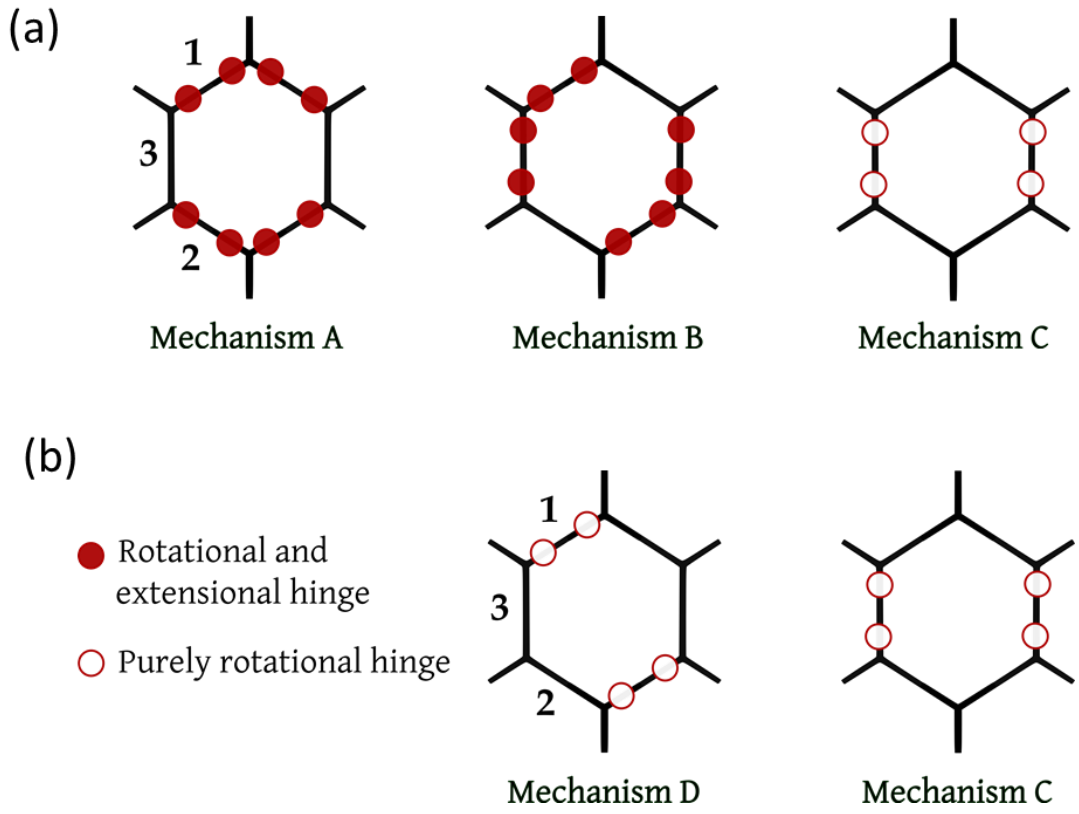


Fig. 4. The collapse modes that define the yield surface for (a) $\omega \neq 30^o$ and (b) $\omega = 30^o$.

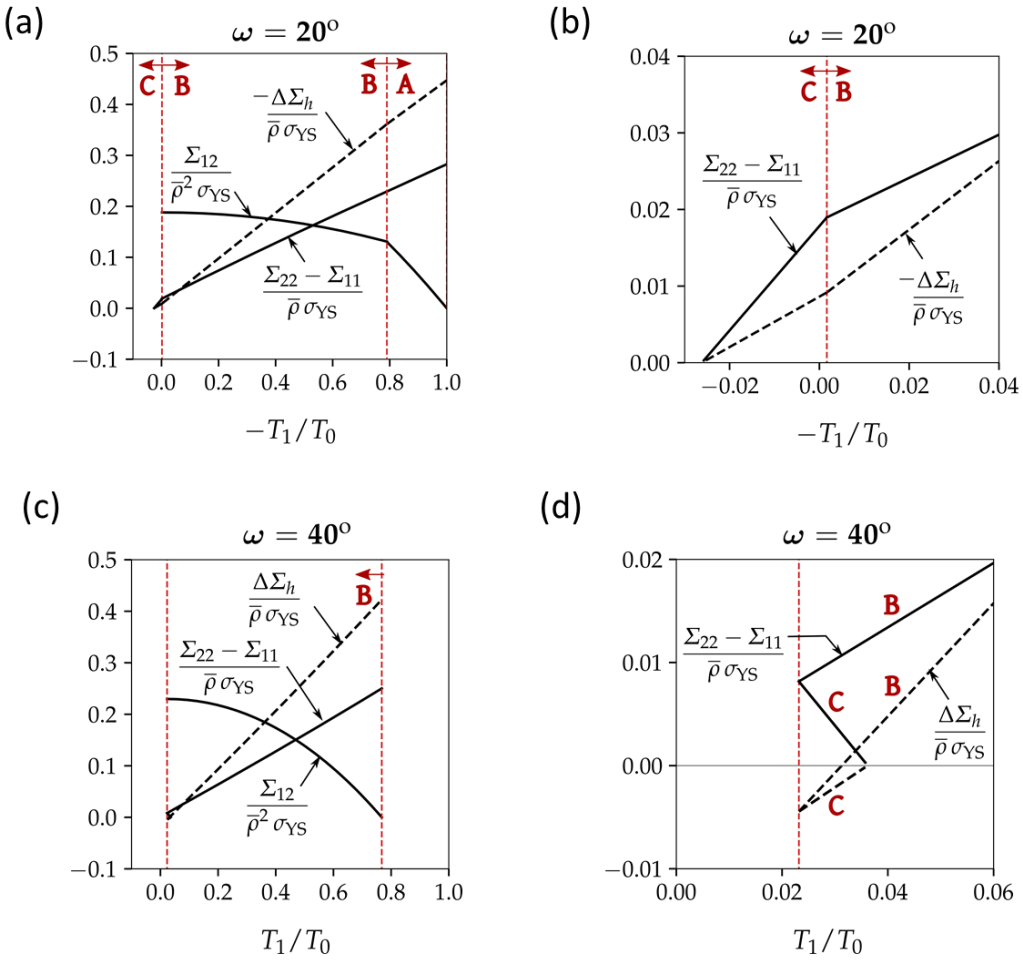


Fig. 5. Generation of the yield surface by varying $T_1/T_0$, for (a, b) $\omega = 20^o$ and (c, d) $\omega = 40^o$. Zoomed-in portions of (a) and (c) are shown in (b) and (d), respectively, to reveal the transition between mechanisms B and C. The labels A, B and C indicate the regime of dominance of mechanisms A, B and C, respectively.

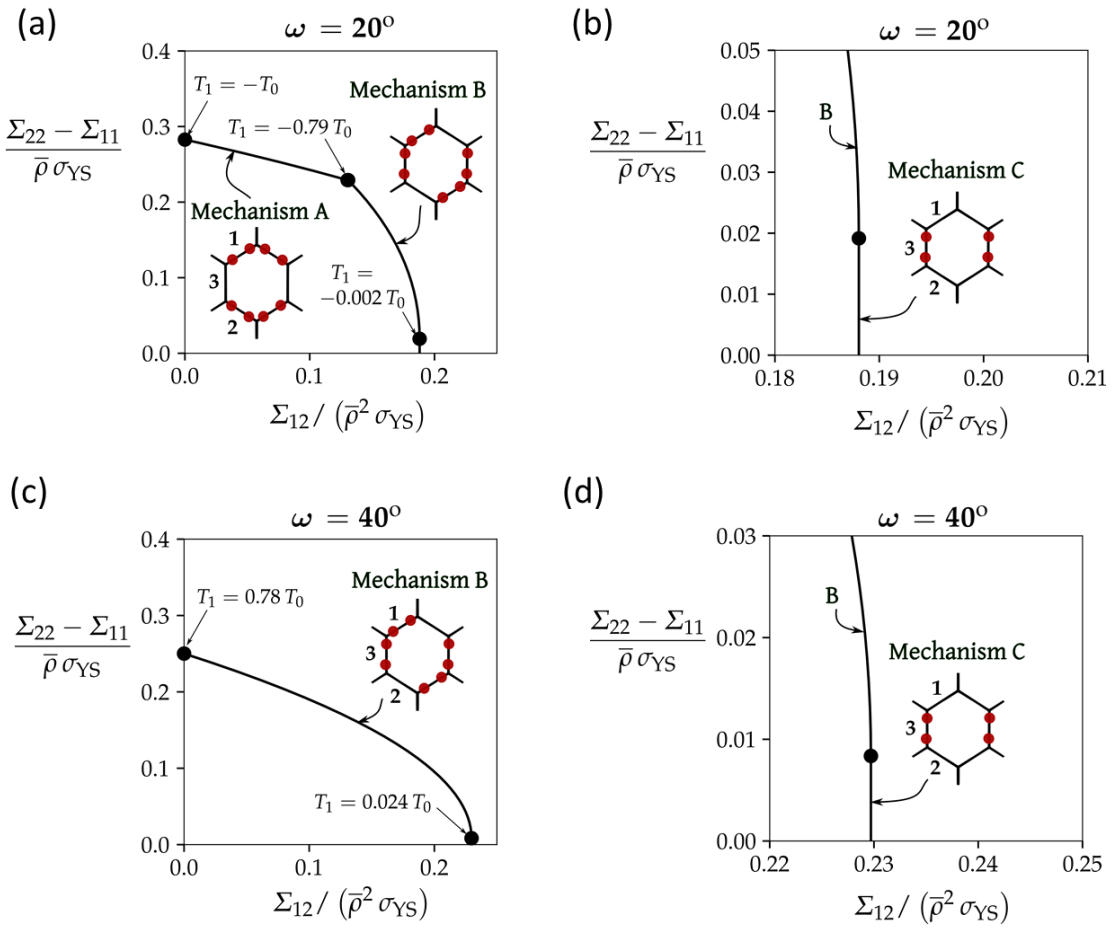


Fig. 6. The yield surface and the active mechanisms for $\bar{\rho} = 0.05$. (a) $\omega = 20^{\circ}$ and (b) $\omega = 20^{\circ}$, enlarged view near shear axis; (c) $\omega = 40^{\circ}$ and (d) $\omega = 40^{\circ}$, enlarged view near shear axis.

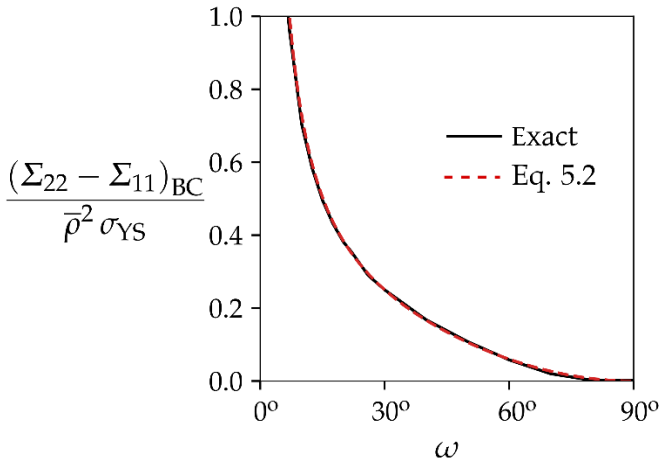


Fig. 7. Dependence of transition value of $(\Sigma_{22} - \Sigma_{11})_{BC}$ for mechanisms B and C upon bar inclination $\omega$, for $\bar{\rho} = 0.05$.

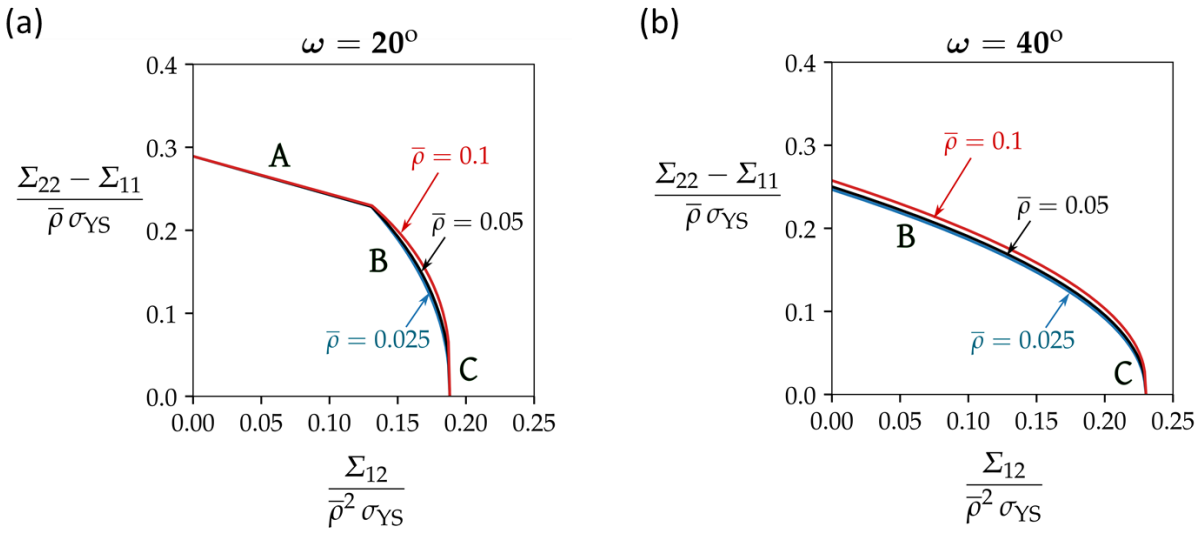


Fig. 8. Sensitivity of yield surface shape to relative density $\bar{\rho}$ for (a) $\omega = 20^{o}$ and (b) $\omega = 40^{o}$.

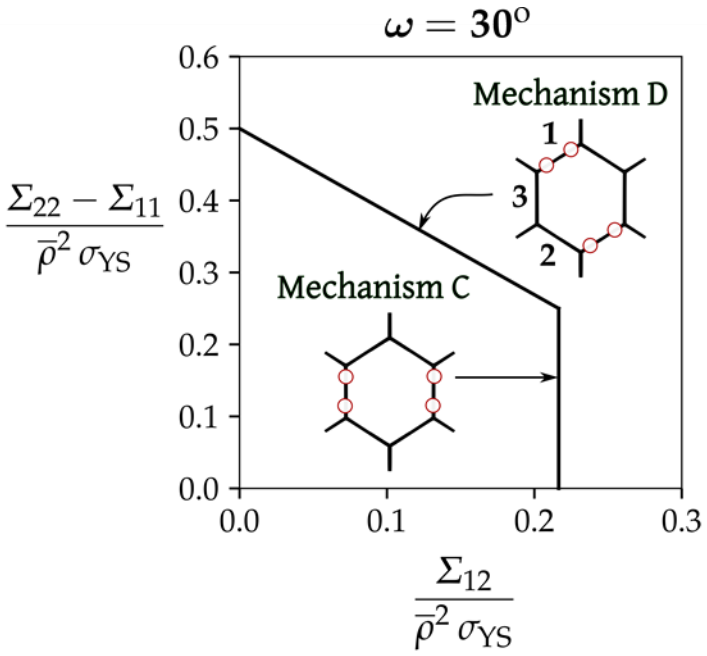


Fig. 9. Collapse surface for the singular case of a regular honeycomb, with $\omega = 30^{o}$.

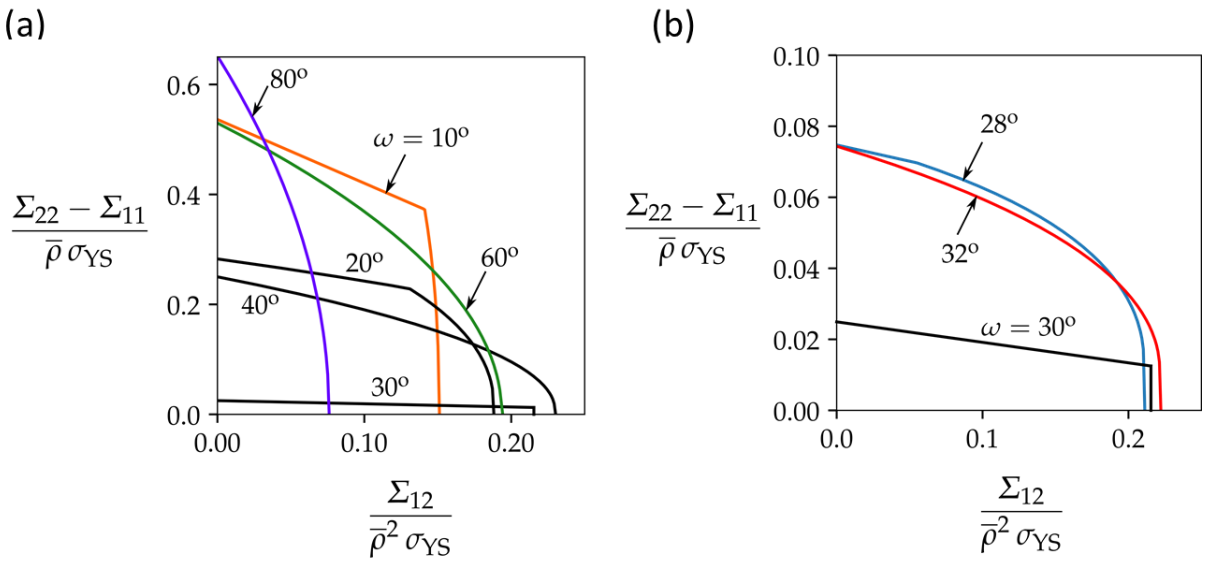


Fig. 10. (a) yield surface for a wide range of values of bar inclination $\omega$, for $\bar{\rho} = 0.05$. (b) yield surface size for $\omega$ in the vicinity of $\omega = 30^{o}$, again for $\bar{\rho} = 0.05$

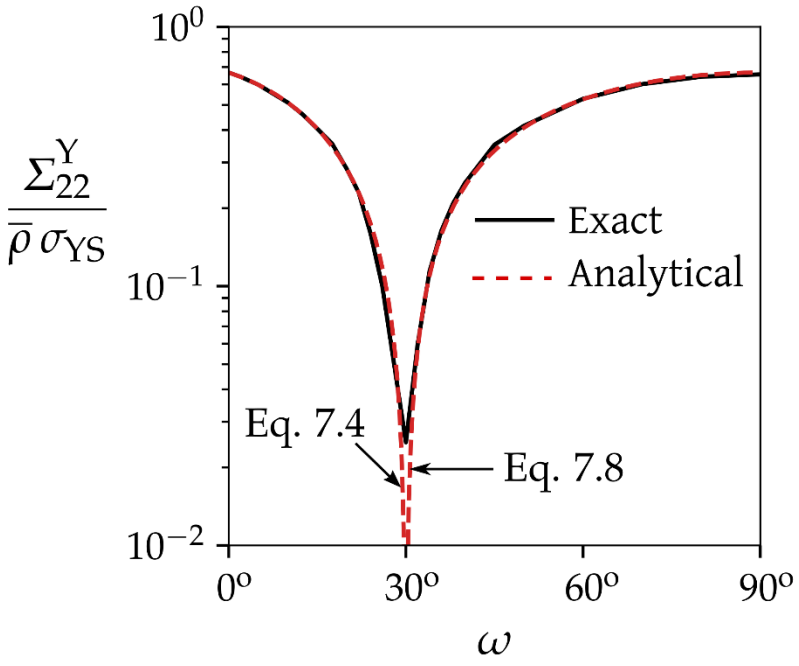


Fig. 11. Dependence of uniaxial tensile strength upon bar inclination $\omega$. The relative density is $\bar{\rho} = 0.05$ for the exact solution.

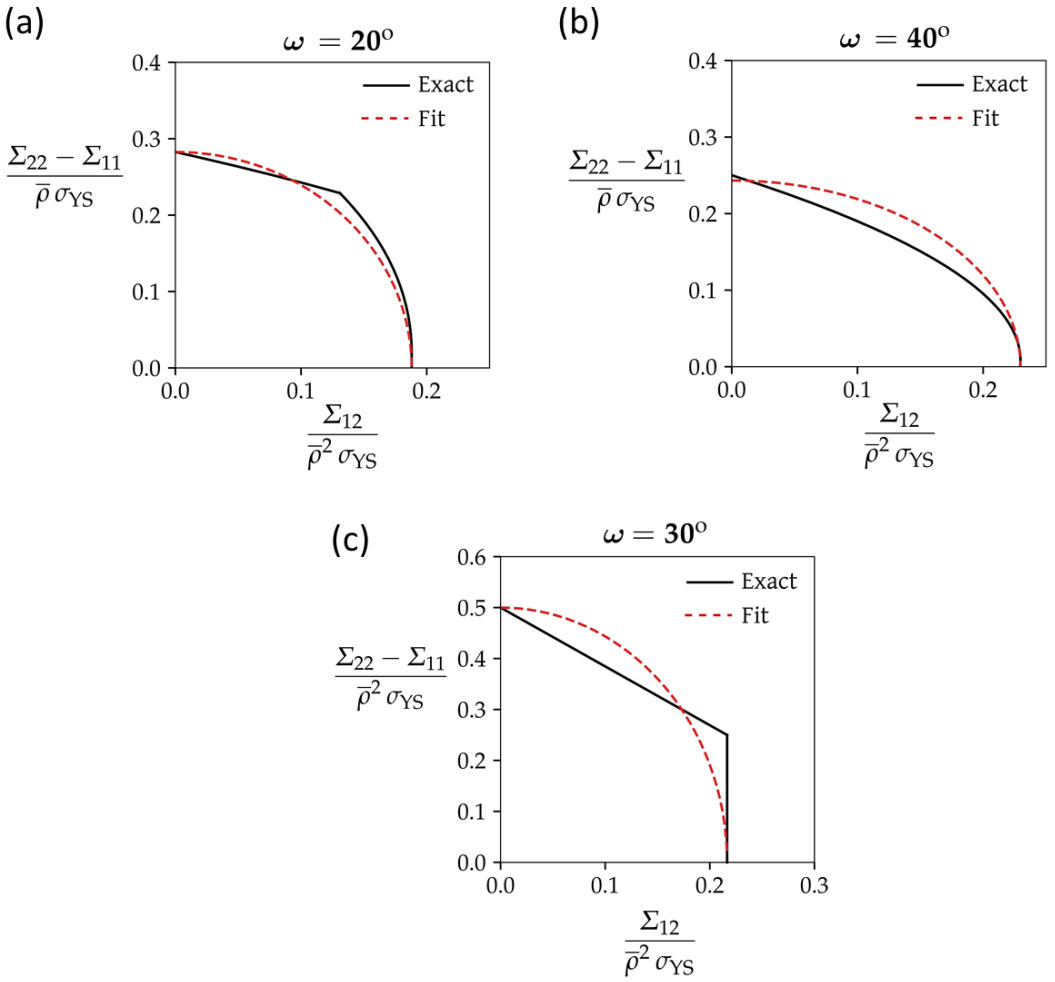


Fig. 12. Approximate fit to the yield surface by an ellipse for (a) $\omega = 20^o$, (b) $\omega = 40^o$ and (c) $\omega = 30^o$. The relative density is $\bar{\rho} = 0.05$ in (a) and (b).